A Unified Design Approach of Optimal Transient Single-Phase-Shift Modulation for Nonresonant Dual-Active-Bridge Converter With Complete Transient DC-Offset Elimination

Chuan Sun ⓘ, *Student Member, IEEE*, Xingyue Jiang ⓘ, Junwei Liu ⓘ, *Member, IEEE*, Lingling Cao ⓘ, *Member, IEEE*, Yongheng Yang ⓘ, *Senior Member, IEEE*, and K. H. Loo ⓘ, *Member, IEEE*

Abstract—The dynamics of nonresonant dual-active-bridge converter (DABC) are simultaneously affected by the transient modulation strategy and controller design. In general, inappropriate transient modulation strategies can lead to nonzero transient dc offsets in the inductor current and transformer's magnetizing current, thus introducing excessive trajectory tracking error and time delays between the pulsewidth modulation generator and controller. Consequently, truly optimal transient responses cannot be achieved solely through a high-performance controller, unless the modulation-induced transient dc offsets can be completely eliminated. This article presents a comprehensive review of the optimized transient phase-shift modulation (OTPSM) strategies for single-phase-shift modulated DABC, and derives a novel optimal modulation method referred to as symmetric single-sided OTPSM (SS-OTPSM), which is based on a unified theoretical framework of OTPSM and an additional condition enabling a full elimination of all undesired transient dc offsets. The proposed SS-OTPSM can be easily and cost-effectively implemented in a cycle-by-cycle manner, and inherently compatible with fast controllers. Additionally, in order to more accurately match DABC's power transfer model under SS-OTPSM, an enhanced model predictive controller (EMPC) is proposed. By a combined use of SS-OTPSM and EMPC, ultrafast and completely dc-offset-free dynamics can be achieved without measuring the inductor current. The effectiveness of the proposed schemes is verified by closed-loop simulation and experimental results.

Index Terms—DC offset, dual-active-bridge (DAB), fast transient response, model predictive control, phase-shift modulation.

I. INTRODUCTION

AS an attractive bidirectional dc–dc topology, nonresonant dual-active-bridge converter (DABC) is widely used in various industry applications [1]. Besides transmitting electric power with high efficiency, DABC is increasingly required to demonstrate fast dynamics and offer robust output voltage regulation under complex load conditions, such as pulsed-power loads [2]. Meanwhile, fast dynamics are indispensable to reduce output filter size, which enables more compact system integration.

It can be found from recent overview studies [3], [4] that the technological improvements in the dynamics of DABC have been achieved mainly through advanced controller design. In these cases, the adverse effects caused by inappropriate transient phase-shift modulation strategies under closed-loop conditions have been ignored. In fact, transient modulation strategies can significantly affect the dynamics of DABC, since any changes in the inductor current are eventually accomplished through a sequence of switching actions, i.e., modulation. For example, even with a well-designed controller, the application of conventional transient phase-shift modulation (CTPSM) will lead to excessive transient dc offsets accompanied by significant overshoots/undershoots in both the inductor current and transformer's magnetizing current. This can further lead to long settling time, high-current stresses on power devices, and risk of magnetic saturation [5], and ultimately give rise to inductor-current trajectory tracking error and time delays between the pulsewidth modulation (PWM) generator and controller, thus degrading the overall dynamics of DABC. As a consequence, it is difficult to achieve optimal dynamic performance only by optimizing controller without co-optimizing transient phase-shift modulation strategy. Unfortunately, the influence of transient modulation on closed-loop controlled DABC remains underexplored and, thus, is not well understood, and most of the existing

Chuan Sun, Xingyue Jiang, Junwei Liu, and K. H. Loo are with the Department of Electronic and Information Engineering, The Hong Kong Polytechnic University, 999077, Hong Kong (e-mail: chuan.sun@connect.polyu.hk; xingyue.jiang@connect.polyu.hk; liujunwei_hust@hotmail.com; kh.loo@polyu.edu.hk).

Lingling Cao is with the School of Mechanical Engineering and Automation, Harbin Institute of Technology, Shenzhen, Guangdong 518055, China (e-mail: caolingling@hit.edu.cn).

Yongheng Yang is with the College of Electrical Engineering, Zhejiang University, Hangzhou 310027, China (e-mail: yang_yh@zju.edu.cn).

studies do not consider the impacts of these two factors (i.e., controller and transient modulation), simultaneously.

A. Literature Review on Optimized Transient Phase-Shift Modulation (OTPSM) Strategies for DABC

In order to eliminate transient dc offsets, various OTPSM strategies have been proposed for both single-phase-shift (SPS) modulated DABC [6]–[19] and multi-phase-shift (MPS) modulated DABC [20]–[24]. The advantage of OTPSM is the ability to directly update a large-amplitude phase-shift increment/decrement within about one switching cycle and to limit inductor current as a protective measure. Despite slight design differences, the common principle of such OTPSM strategies is to design specific switching sequences that can seamlessly modify the trajectory of inductor current during transient state. According to the analysis presented in [24], the transient dc-offset elimination under MPS modulation schemes can be achieved through generating suitably designed square-wave voltage in each half-bridge leg of DABC. Hence, the theories of OTPSM developed for SPS modulation will form the basis for developing more advanced OTPSM strategies based on MPS modulation. In Section III-B, a comprehensive review of the prior-art SPS modulation based OTPSM strategies [6]–[19] is presented. Although, in theory, they can help us to improve the dynamics of DABC, they have several limitations, as follows.

1) Previous studies have failed to explore the underlying relationships between different types of OTPSM, leading to the development of numerous variants of similar methods.
2) The existing OTPSM strategies cannot achieve complete transient dc-offset elimination, as the average values of both the inductor current and transformer's magnetizing current are still nonzero during transient state. In addition, transient overshoots or undershoots can be observed in transformer's magnetizing current.
3) Owing to the high implementation complexity of dynamically applying existing OTPSM strategies in the PWM generator, their effectiveness is not yet verified in a fast closed-loop controlled DABC. As can be observed from the simulation and experimental results in almost all of these previous studies except [16], most of the existing OTPSM strategies have only been validated in open-loop conditions, in which these strategies only need to be executed once instead of on a cycle-by-cycle basis.
4) A much-debated question is whether such OTPSM strategies can truly bring about a positive effect on improving the dynamics of closed-loop controlled DABC. An OTPSM strategy proposed in [16] was verified with a single-loop voltage-mode proportional-integral (PI) controller. In order to demonstrate the benefit of the use of OTPSM, the gain of PI controller has to be significantly increased for generating large step changes in phase-shift ratio. However, since a pure PI controller typically suffers from the tradeoff between response time and stability margins, the results under PI controller plus OTPSM remained unsatisfactory, and the converter tended to become unstable under PI controller plus CTPSM. This implies

that the combined use of OTPSM with a PI controller cannot fully deliver the anticipated dynamic performance, and such low-gain linear controllers are not effective to be used with OTPSM.

Overall, previous studies of OTPSM have exhibited limitation in their failure to achieve zero transient dc offsets. Besides, their effectiveness when applied to fast closed-loop controlled DABC is not verified. The inadequacy of using a PI controller in realizing the full potential of OTPSM strategies is evident but its replacement by other more advanced high-gain controllers such as a model predictive controller (MPC) remains largely underexplored, thus preventing OTPSM from realizing its full benefits.

B. Literature Review on Fast Control Schemes for DABC

Recently, fast MPC has been extensively studied due to its outstanding dynamic performance and ease of use [2], [25], [26]. Compared with conventional PI controller [27], its response time and output voltage fluctuation can be significantly reduced. However, since the controller gain of a fast MPC is high, the control variable (i.e., phase-shift ratio) will undergo large-magnitude changes during transient state. Typically, under CTPSM, the higher the controller gain is, the larger the dc offsets become. In order to limit the peak inductor current within a tolerance band, practical fast controllers are often integrated with specified constraint conditions or antiwindup design. For example, in [26], an additional constraint on the inductor current is imposed by the MPC algorithm, but this inevitably shrinks the controller's bandwidth. Consequently, fast dynamics cannot be fully realized with MPC+CTPSM, and new fast control scheme needs to be devised.

Conventionally, to achieve fast dynamics without introducing excessive transient dc offsets, several control techniques were presented, e.g., peak-current-mode control [28], natural-switching-surface-based boundary control [29], current-mode feed-forward control [30], [31], and deadbeat current control [32]. Unfortunately, although all of them can actively clamp the envelope of the inductor current, and respond to large-amplitude disturbances rapidly, they are not desirable solutions because high-frequency ac-link waveforms (e.g., the inductor current) must be sampled by costly high-bandwidth sensors at a high sampling rate, making them unsuitable for high-frequency operated DABC. However, the literature has rarely discussed solutions that can adequately resolve the contradiction between fast control and dc offsets in closed-loop controlled DABC without measuring the inductor current.

C. Main Contributions of This Article

In light of the abovementioned, it is necessary to integrate a fast controller (e.g., MPC) with a sensorless OTPSM strategy, such that the potential risk of modulation-induced dc offsets in fast closed-loop controlled DABC can be mitigated without measuring the inductor current and the aforesaid limitations of PI+OTPSM and MPC+CTPSM can also be overcome.

By studying the inherent operating principles of OTPSM, this article attempts to develop a set of unified equations governing

essentially all the existing OTPSM strategies, and propose a new sensorless method known as symmetric single-sided OTPSM (SS-OTPSM). The proposed SS-OTPSM aims to completely eliminate the transient dc offsets in both inductor current and transformer's magnetizing current simultaneously, thus minimizing their deleterious effects on the dynamics of DABC. To prove the superiority of SS-OTPSM, an in-depth discussion on the mechanisms of different existing OTPSM strategies and comprehensive comparisons between them are presented. It is found that SS-OTPSM exhibits a significantly better performance in terms of transient dc-offset elimination in all open-loop cases.

Benefiting from its symmetrical transient switching patterns, it is easy to implement SS-OTPSM in a cycle-by-cycle manner, thus facilitating its closed-loop realization and making it highly practical over existing OTPSM strategies. To examine the validity of SS-OTPSM in closed-loop conditions, different combinations of transient modulation strategies and MPCs are compared systematically. In addition, an enhanced model predictive controller (EMPC), which is designed with specific compatible characteristics with SS-OTPSM, is proposed to achieve optimal (i.e., ultrafast and completely dc-offset-free) dynamics of DABC. The advantages of MPC+SS-OTPSM and EMPC+SS-OTPSM are verified experimentally.

The rest of this article is organized as follows. Section II derives the equivalent circuit and power transfer model of DABC. Different existing OTPSM strategies are discussed in Section III. The principle of the proposed SS-OTPSM strategy is presented in Section IV. Section V presents the design of the proposed EMPC algorithm. Experimental results are shown in Section VI to verify the performance of the proposed SS-OTPSM and EMPC. Finally, Section VII concludes this article.

II. EQUIVALENT CIRCUIT AND POWER TRANSFER MODEL OF DABC

A generic closed-loop control architecture for DABC is shown in Fig. 1. V_1 and V_2 are the input and output voltages, respectively. i_1 and i_2 are the terminal currents of the two full-bridge converters, where i_2 is filtered by an output capacitor C_o to produce a dc load current I_o. The turns ratio of the transformer is $N:1$, and the primary-referred magnetizing inductance is L_m. L_p and L_s are energy transfer elements consisting of the auxiliary inductances and the transformer's leakage inductances. i_L (inductor current) and i_M (magnetizing current) are defined as the currents passing through L_p and L_m, respectively. R_s is the equivalent series resistance (ESR) of the circuit, which is ignored in the analysis. v_{ab} and v_{cd} are two high-frequency square-wave voltages produced by the primary-side full-bridge converter comprising switches S_1–S_4 and the secondary-side full-bridge converter formed by switches Q_1–Q_4, respectively, and they are phase-shifted by a ratio D to determine the direction and amount of power flow.

Fig. 2 shows the primary-referred equivalent circuits of the DABC. Fig. 2(a) represents an ideal DABC, where the magnetizing inductance is assumed to be much larger than the total equivalent series inductance $L = L_p + N^2 L_s$, while Fig. 2(b)
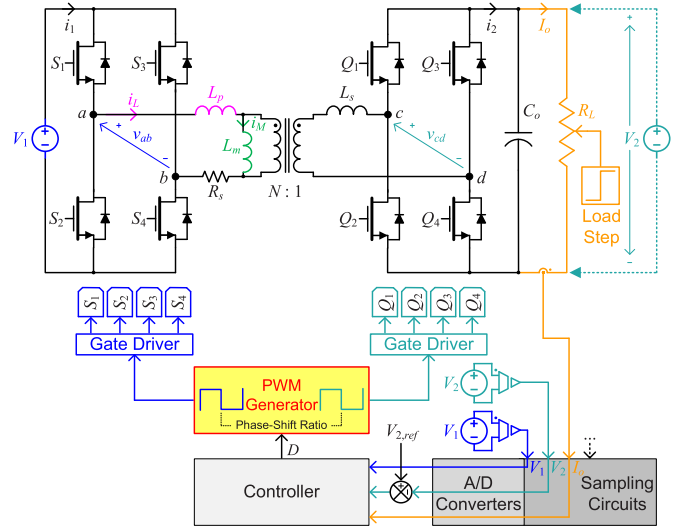

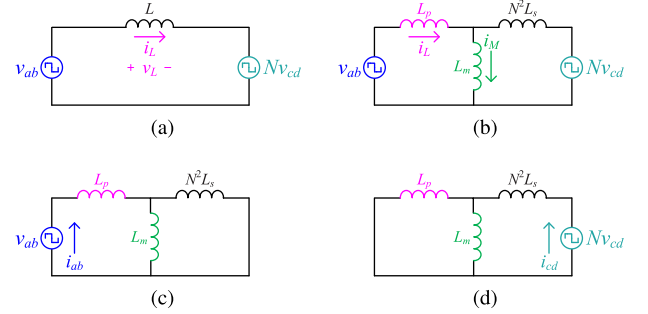Fig. 1. Generic closed-loop control architecture for nonresonant DABC.

Fig. 2. Primary-referred equivalent circuits of nonresonant DABC. (a) Ideal equivalent circuit. (b) T-model equivalent circuit. Applying superposition principle. (c) Individual contribution due to v_{ab}. (d) Individual contribution due to Nv_{cd}.

includes L_m by adopting the transformer's T equivalent model (T-model). Applying superposition principle to Fig. 2(b) gives Fig. 2(c) and (d). Thus, i_L and i_M can be expressed as

$$i_L = i_{ab} - \frac{L_m}{L_m + L_p} i_{cd} \qquad (1)$$

$$i_M = \frac{N^2 L_s}{L_m + N^2 L_s} i_{ab} + \frac{L_p}{L_m + L_p} i_{cd} \qquad (2)$$

where i_{ab} and i_{cd} are the current contributions due to each independent source (v_{ab} or v_{cd}) acting alone. This implies that i_L and i_M are functions of i_{ab} and i_{cd}, and their waveforms can be determined by applying superposition and analyzing the single-source equivalent circuits in Fig. 2(c) and (d). In order to measure i_M, an additional inductor whose inductance is equal to the transformer's magnetizing inductance is connected across the transformer's primary terminal. By directly measuring the current through this additional inductor, i_M will be replaced with i_M' in all the following simulation and experimental tests, where $i_M' \approx 0.5 i_M$.
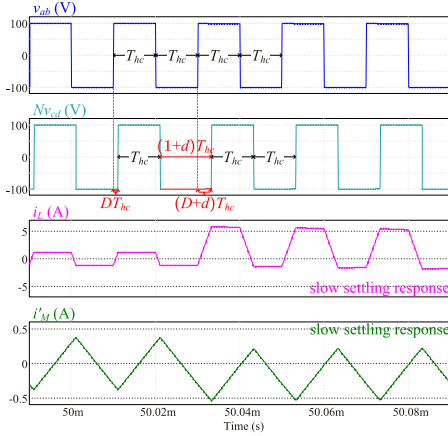
Fig. 3. Simulated open-loop transient response for an increase in the phase-shift ratio from $\frac{1}{9}$ to $\frac{1}{3}$ under CTPSM.

In general, $L_m \gg L_p$, and thus, (1) can be approximated as

$$i_L \approx i_{ab} - i_{cd}. \tag{3}$$

The average power transferred to the output/load can be computed from

$$P = \frac{1}{2T_{\text{hc}}} \int_0^{2T_{\text{hc}}} v_{ab}(t) i_L(t) \mathrm{d}t \approx \frac{NV_1 V_2 T_{\text{hc}} D(1-D)}{L} \tag{4}$$

where T_{hc} is one-half of the switching period. It should be pointed out that (4) represents the ideal power transfer model, which does not consider dead-time effect, which could lead to phase-shift error particularly at light load [33]. According to [34], dead-time compensation methods can be easily integrated with OTPSM strategies, if necessary. Furthermore, the error in phase-shift ratio induced by dead-time effect can be automatically compensated by a closed-loop controller. Hence, dead-time effect is neglected in the following discussion.

III. EXISTING TRANSIENT MODULATION STRATEGIES FOR SPS MODULATED DABC

Upon receiving the signal for power adjustment from controller following a load change, the phase-shift ratio between v_{ab} and v_{cd} should be updated from its current value $D[n] = D$ to the desired (next) value $D[n+1] = D + d$, where d is the phase increment or decrement. It is the responsibility of PWM generator to specify the way to update d.

A. CTPSM Strategy

CTPSM is the default method implemented by the PWM modules of most commercial microprocessors. The operating mechanism of CTPSM can be demonstrated by a simulation example presented in Fig. 3. In order to update the phase-shift ratio, the low-level duration of v_{cd} will be updated to $(1 + d)T_{\text{hc}}$ during transient state, while both v_{ab} and v_{cd} will maintain a constant high-level duration of T_{hc}. Under CTPSM, noticeable transient dc offsets will appear in all related voltage and current waveforms (e.g., i_2, V_2, i_L, and i_M). This problem arises from the fact that any asymmetry in the inductor volt-second product

will give rise to magnetic flux imbalance that induces dc offsets, and hence, the directly-adjusted transient switching pattern under CTPSM will lead to a monotonic increase in the volt-second product applied to the inductor during transient state. Since inductors cannot dissipate energy, the excess energy can only be absorbed by the parasitic resistance R_s slowly. In general, the first peaks of the transient waveforms are much higher than the new steady-state values, and it will take several cycles before the transient waveforms stabilize, thus resulting in a large, negative impact on the transient performance of DABC. Obviously, such dc offsets cannot be eliminated by means of controller design as they are generated by the inappropriate switching sequence of the PWM generator. For this reason, CTPSM is undesirable and should be replaced by more advanced and appropriately designed transient modulation strategies.

B. Existing OTPSM Strategies

When subjected to fast changes in phase-shift ratio, the OTPSM strategies reported in [6]–[19] can achieve smooth transition response by designing optimized transient switching sequences. According to their modulation characteristics and degrees of freedom (DOF), characterized in terms of the number of adjustable positive and negative pulse widths during transient state, they can be classified into six categories, i.e., Types A–F. Note that the numeric subscripts attached to the type names (e.g., number 1 in A_1) are used to define different subtypes. One simulation example of each type of OTPSM can be found in Fig. 4, where the red line segments are the transient pulses that need to be adjusted and the measured transient average value (TAV) of i_L or i'_M is also labeled.

Type-A OTPSM [6]–[10] and Type-B OTPSM [10]–[12] strategies originate from the principle of relative motion. Specifically, two or three edges are selected from v_{ab} and v_{cd} to asymmetrically distribute the total required phase-shift adjustment in order to achieve the desired peak value of i_L corresponding to the new steady state. For example, in Fig. 4(a), the falling edge of v_{ab} and the rising edge of v_{cd} will move toward each other. However, as depicted in Fig. 4(a) (Type A_1 [6]) and (b) (Type B_1 [10]), although i_L can reach its new steady state within one switching cycle, excessive transient dc offset and long settling time are still exhibited by i_M, since the volt-second products on L_M under Type-A and Type-B OTPSM strategies are adjusted unevenly in resemblance to CTPSM. In addition, the transient pulse widths under these two types of OTPSM strategies are related to the voltage gain M of DABC, where $M = NV_2/V_1$. Hence, they are sensitive to converter parameters such as N, V_1, and V_2.

In contrast to the abovementioned two OTPSM strategies, the transient pulse widths of Type-C OTPSM [10], [13], Type-D OTPSM [14], [15], Type-E OTPSM [13], [16], and Type-F OTPSM [16]–[19] strategies are independent of M and determined only by D and d, and both i_L and i_M can reach their new steady states within one switching cycle. As exemplified in Fig. 4(c) (Type C_1 [13]), (d) (Type D_1 [14]), and (e) (Type E_1 [16]), Type-C and Type-E OTPSM strategies generate two equal-width transient pulses by consecutively moving two edges
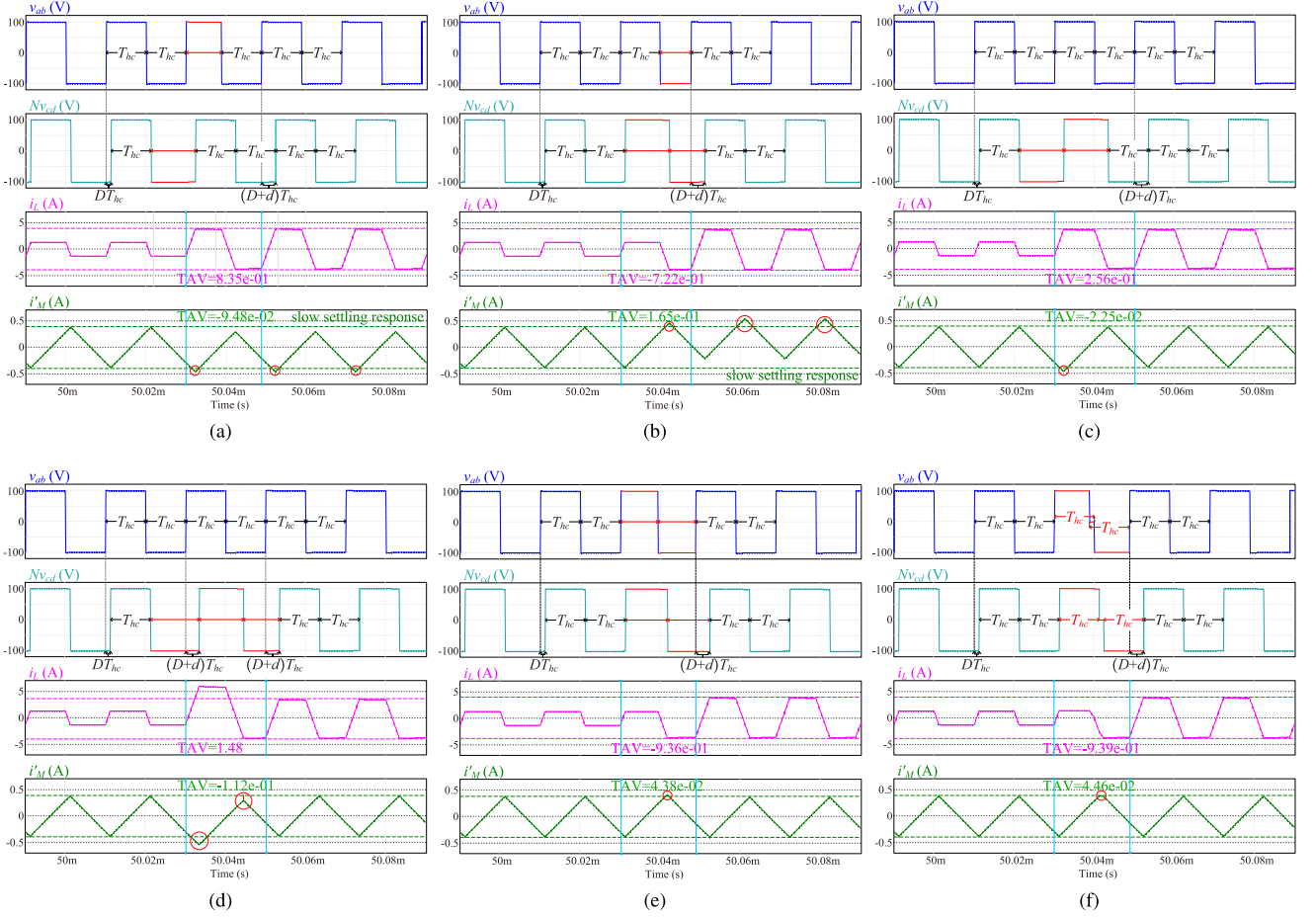
Fig. 4. Simulated open-loop transient response for an increase in the phase-shift ratio from $\frac{1}{9}$ to $\frac{1}{3}$ under different types of OTPSM strategies. (a) Type A_1 [6]. (b) Type B_1 [10]. (c) Type C_1 [13]. (d) Type D_1 [14]. (e) Type E_1 [16]. (f) Type F_1 [16].
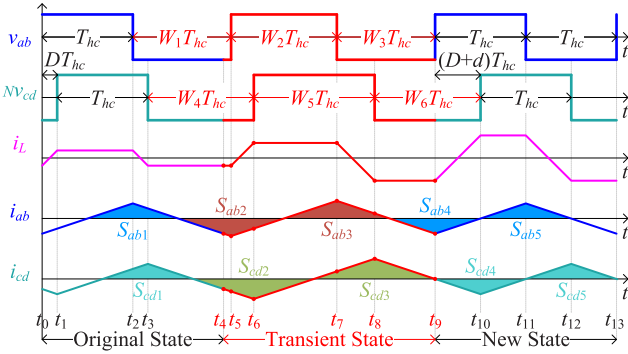

Fig. 5. Unified framework for OTPSM strategies.

of v_{ab} and/or v_{cd}, while Type-D OTPSM strategies continuously generate three unequal-width transient pulses in v_{cd}. Unlike the abovementioned OTPSM strategies, as exemplified in Fig. 4(f) (Type F_1 [16]), Type-F OTPSM introduces zerovoltage durations into v_{ab} and/or v_{cd} during transient state, so that v_{ab} and/or v_{cd} become three-level voltages and the diagonal switches should be phase-shifted, which increases the complexity of its implementation. Unfortunately, according to

the simulation results presented in Fig. 4, it should be specially noted that all Type-C to Type-F OTPSM strategies can lead to overshoots/undershoots in i_M, and the average values of both i_L and i_M during transient state are not zero.

In summary, although the settling time of i_L and/or i_M can be shortened by existing OTPSM strategies, due to their inherent design limitation, all of these strategies are unable to achieve zero dc offsets in both i_L and i_M during transient state. As a result, the adverse effects induced by transient dc offsets cannot be effectively mitigated by such existing OTPSM strategies, when they are implemented in a cycle-by-cycle manner. Eventually, since the nonzero transient dc offsets can appear at i_2 and I_o, the transient performance of closed-loop controlled DABC will be degraded. Therefore, a new OTPSM scheme is required to completely eliminate the transient dc offsets and make it more practical for closed-loop applications.

IV. PROPOSED SYMMETRIC SS-OTPSM STRATEGY

A. Dynamic Volt-Second Balance

The previous section has shown that the basic operation of Type-A to Type-E OTPSM strategies is characterized by
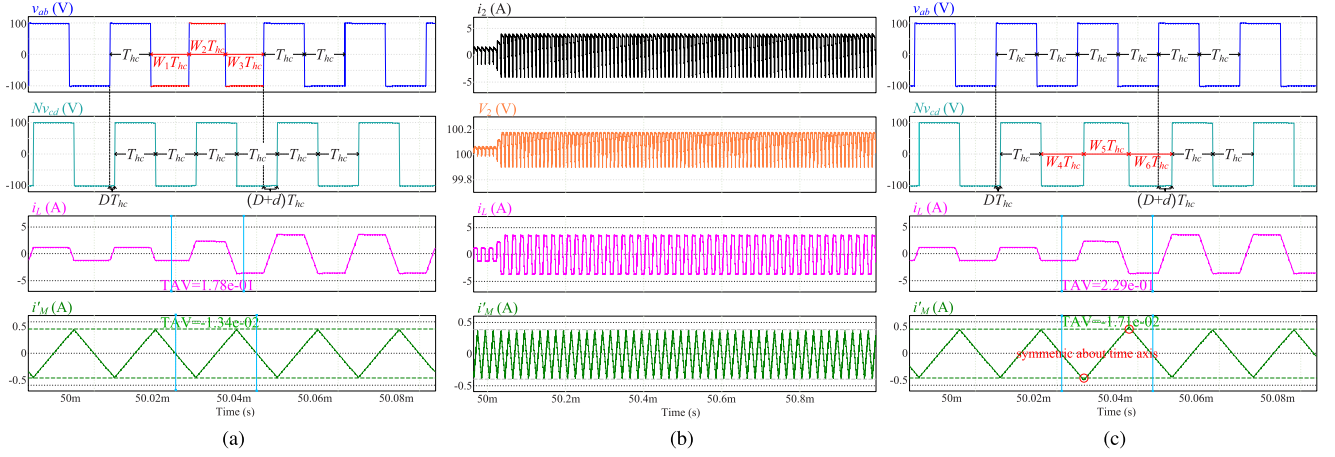
Fig. 6. Simulated open-loop transient response for an increase in the phase-shift ratio from $\frac{1}{9}$ to $\frac{1}{3}$ under SS-OTPSM strategies. (a) Main waveforms under Type-I SS-OTPSM. (b) Zoomed-out waveforms of i_2, V_2, i_L, and i_M under Type-I SS-OTPSM. (c) Main waveforms under Type-II SS-OTPSM.
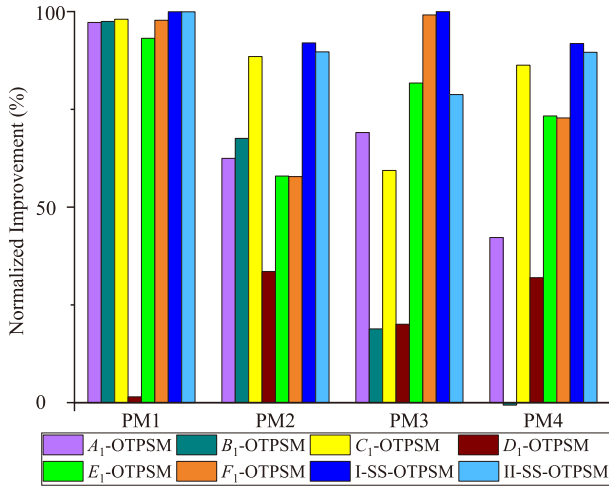

Fig. 7. Normalized performance evaluation of different OTPSM strategies in open-loop simulations for an increase in the phase-shift ratio from $\frac{1}{9}$ to $\frac{1}{3}$.
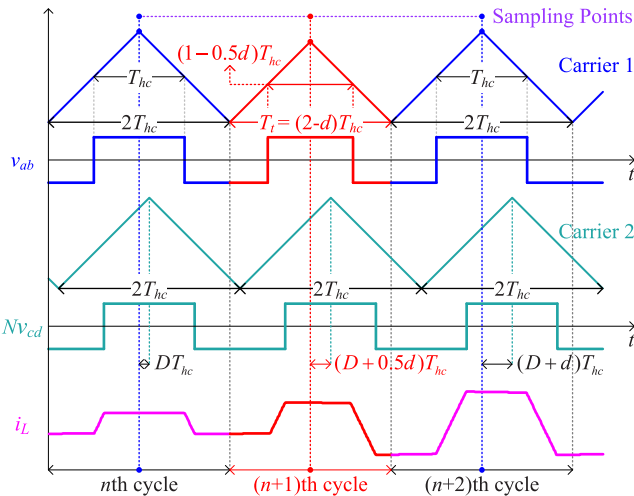

Fig. 8. Implementation details of Type-I SS-OTPSM on the PWM modules of a microprocessor platform.

appropriately adjusting some of the positive and negative pulse widths of the two-level voltages (v_{ab} and v_{cd}) during transient state for meeting the dynamic volt-second balance requirement in the series inductor. To achieve this, as can be seen from Fig. 5, there are in fact up to six transient pulsewidth ratios, i.e., W_1–W_6, which can be manipulated in the waveforms of v_{ab} and v_{cd}. Once the transient trajectory of i_L is successfully modified (by modulating W_1–W_6) to reach its new steady-state trajectory, i_L will enter and remain in the new periodic steady state indefinitely until the next transient event occurs. Typically, for all the previously mentioned OTPSM strategies, i_L will reach its new steady state in about one switching cycle, i.e., no later than t_9. This means that the problem encountered in designing OTPSM is to find the closed-form solutions for W_1–W_6 that will satisfy the boundary conditions at t_9:

1) *Constraint* 1: The phase-shift ratio between the rising edges of v_{ab} and v_{cd} must be equal to $D + d$ at the end of the transient state, i.e., the time interval $t_{10} - t_9 = (t_{10} - t_0) - (t_9 - t_0) = (D + 1 + W_4 + W_5 + W_6)T_{hc} - (1 + W_1 + W_2 + W_3)T_{hc}$ should be equal to $(D + d)T_{hc}$. Hence,

$$W_1 + W_2 + W_3 + d = W_4 + W_5 + W_6. \quad (5)$$

2) *Constraint* 2: The end point of the transient state is the initial point of the new steady-state cycle. Hence,

$$i_L(t_9) = i_L(t_{13}). \quad (6)$$

In general, the key objective of OTPSM is to determine the solution sets for the unknown modulation parameters W_1–W_6 based on the abovementioned two constraints.

Referring to [6], the boundary values of i_L in the original steady state (from t_0 to t_4) and new steady state (from t_9 to t_{13}), namely, $i_L(t_0)$, $i_L(t_4)$, and $i_L(t_{13})$, are given by

$$i_L(t_0) = i_L(t_4) = -\frac{T_{hc}}{2L}[V_1 + (2D - 1)NV_2] \quad (7)$$

$$i_L(t_{13}) = -\frac{T_{hc}}{2L}[V_1 + (2(D + d) - 1)NV_2]. \quad (8)$$

TABLE I
MAIN FEATURES OF DIFFERENT TRANSIENT PHASE-SHIFT MODULATION STRATEGIES

Type	DOF	Reference	W1	W2	W3	W4	W5	W6	Sensorless	Complexity	CE†
CTPSM	1	—	1	1	1	$1+d$	1	1	Yes	★	No
A_1 OTPSM	2	[6]	1	$1-\frac{dM}{M+1}$	1	$1+\frac{d}{M+1}$	1	1	No	★★★	No
A_2 OTPSM	2	[7]	1	1	$1-\frac{dM}{M+1}$	1	$1+\frac{d}{M+1}$	1	No	★★★	No
A_3 OTPSM	2	[7]	1	$1-\frac{dM}{M-1}$	1	1	$1-\frac{d}{M-1}$	1	No	★★★	No
A_4 OTPSM	2	[7]	1	1	$1-\frac{dM}{M-1}$	1	1	$1-\frac{d}{M-1}$	No	★★★	No
A_5 OTPSM	2	[8]	1	1	1	$1+\frac{d}{M+1}$	$1+\frac{dM}{M+1}$	1	No	★★★	No
A_6 OTPSM§	2	[9]	1 / 1	1 / 1	$1-\frac{d+2}{M+1}$ / $1-\frac{d-2}{M+1}$	1 / 1	$1+\frac{(d+2)M}{M+1}$ / $1+\frac{(d-2)M}{M+1}$	1 / 1	No	★★★★	No
A_7 OTPSM	2	[10]	$1-\frac{dM}{M-1}$	1	1	$1-\frac{d}{M-1}$	1	1	No	★★★	No
B_1 OTPSM	3	[10]	1	1	$1-d$	1	$1+\frac{d}{2M}$	$1-\frac{d}{2M}$	No	★★★★	No
B_2 OTPSM	3	[10]	1	$1+\frac{dM}{2}$	$1-\frac{dM}{2}$	1	$1+d$	1	No	★★★★	No
B_3 OTPSM	3	[11]	$1+\frac{\frac{|D+d|}{M}+D}{2}$	$1-\frac{\frac{|D+d|}{M}-D}{2}$	1	1	$1-|D+d|$	1	No	★★★★	No
B_4 OTPSM	3	[12]	$1+\frac{d}{2M}$	$1-\frac{d}{2M}$	1	$1+d$	1	1	No	★★★★	No
B_5 OTPSM	3	[12]	$1-\frac{d}{2M}$	$1+\frac{d}{2M}$	1	1	$1+d$	1	No	★★★★	No
C_1 OTPSM	2	[13]	1	1	1	$1+\frac{d}{2}$	$1+\frac{d}{2}$	1	Yes	★★	IE‡
C_2 OTPSM	2	[10]	$1-\frac{d}{2}$	$1-\frac{d}{2}$	1	1	1	1	Yes	★★	IE‡
D_1 OTPSM	3	[14]	1	1	1	$1+d$	$1+\frac{d}{2}$	$1-\frac{d}{2}$	Yes	★★★	IE‡
D_2 OTPSM	3	[15]	1	1	1	$1+\frac{d(d-2D+4)}{4(d+2)}$	$1+\frac{d}{2}$	$1+\frac{d(d+2D)}{4(d+2)}$	Yes	★★★	IE‡
E_1 OTPSM	4	[16]	1	$1-\frac{d}{4}$	$1-\frac{d}{4}$	1	$1+\frac{d}{4}$	$1+\frac{d}{4}$	Yes	★★★	IE‡
E_2 OTPSM§	4	[13]	$1-\frac{D+d}{2}$ / $1+\frac{D}{2}$	$1-\frac{D+d}{2}$ / $1+\frac{D}{2}$	1 / 1	$1-\frac{D}{2}$ / $1+\frac{D+d}{2}$	$1-\frac{D}{2}$ / $1+\frac{D+d}{2}$	1 / 1	Yes	★★★★	IE‡
F_1 OTPSM	6	[16]	—	—	—	—	—	—	Yes	★★★★★	IE‡
I SS-OTPSM	3	Proposed	$1-\frac{d}{4}$	$1-\frac{d}{2}$	$1-\frac{d}{4}$	1	1	1	Yes	★	Yes
II SS-OTPSM	3	Proposed	1	1	1	$1+\frac{d}{4}$	$1+\frac{d}{2}$	$1+\frac{d}{4}$	Yes	★	Yes

Expressions in the first row satisfy $D > 0$, $d < 0$, and $D + d < 0$, while expressions in the second row satisfy $D < 0$, $d > 0$, and $D + d > 0$.

★ Low ★, Moderate ★★, High ★★★, Very High ★★★★, Extreme ★★★★★.

Complete elimination (CE) of transient dc offsets in both i_L and i_M. Incomplete elimination (IE).

From the voltage–current relationship of the equivalent series inductor L, i.e., $L\frac{di_L(t)}{dt}=v_L=v_{ab}-Nv_{cd}$, where v_L is the equivalent series inductor voltage, the intermediate values of i_L in the time interval $[t_4, t_9]$ can be obtained as

$$
\begin{cases}
i_L(t_5) &= i_L(t_4) + \frac{NV_2-V_1}{L}(t_5 - t_4) \\
i_L(t_6) &= i_L(t_5) + \frac{V_1+NV_2}{L}(t_6 - t_5) \\
i_L(t_7) &= i_L(t_6) + \frac{V_1-NV_2}{L}(t_7 - t_6) \\
i_L(t_8) &= i_L(t_7) - \frac{V_1+NV_2}{L}(t_8 - t_7) \\
i_L(t_9) &= i_L(t_8) + \frac{NV_2-V_1}{L}(t_9 - t_8).
\end{cases}
\tag{9}
$$

As can be observed from Fig. 5, the duration of transient process $[t_4, t_9]$ can be divided into five time intervals

$$
\begin{cases}
t_5 - t_4 &= (W_1 - 1)T_{\text{hc}} \\
t_6 - t_5 &= (W_4 - W_1 + D)T_{\text{hc}} \\
t_7 - t_6 &= (W_1 + W_2 - W_4 - D)T_{\text{hc}} \\
t_8 - t_7 &= (W_4 + W_5 - W_1 - W_2 + D)T_{\text{hc}} \\
t_9 - t_8 &= (W_1 + W_2 + W_3 - W_4 - W_5 - D)T_{\text{hc}}.
\end{cases}
\tag{10}
$$

Substituting (7) and (10) into (9) gives

$$
i_L(t_9) = \frac{T_{\text{hc}}}{2L}[(1 - 2W_1 + 2W_2 - 2W_3)V_1
$$

$$
+ (2W_1 + 2W_2 + 2W_3 - 4W_5 - 1 - 2D)NV_2].
\tag{11}
$$

To satisfy (6) (*Constraint* 2), let (8) be equal to (11), which results in

$$
0 = (2 - 2W_1 + 2W_2 - 2W_3)
$$

$$
+ (2W_1 + 2W_2 + 2W_3 - 4W_5 - 2 + 2d)M.
\tag{12}
$$

A combination of (5) and (12) forms the general solution of OTPSM. In theory, any solution set that can simultaneously satisfy (5) and (12) will make i_L reach a new steady state within one cycle. It can be verified that all Type-A to Type-E OTPSM strategies fulfill these two equations. However, (12) implies that if W_1–W_6 cannot be completely decoupled from M, the transient pulse widths will be adversely affected by the noise and measurement errors in M. As has been pointed out in Section III-B, Type-A and Type-B OTPSM strategies are prone to such problems.

To eliminate the dependence of M, both terms on the right-hand side of (12) should be zero. Hence,

$$
\begin{cases}
1 + W_2 = W_1 + W_3 \\
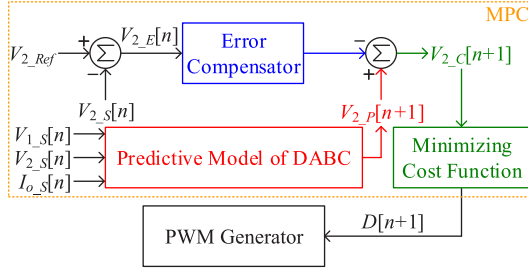W_1 + W_2 + W_3 + d = 1 + 2W_5.
\end{cases}
\tag{13}
$$

Fig. 9. Conceptual block diagram of MPC.

Then, substituting (5) into (13) gives

$$\begin{cases} 1 + W_2 = W_1 + W_3 \\ 1 + W_5 = W_4 + W_6 \\ 2W_2 + d = 2W_5. \end{cases} \tag{14}$$

Since the relationships between W_1 and W_6 described by (14) are decoupled from M, (14) represents a general solution that can be used for developing sensorless (i.e., without being affected by M) OTPSM strategies. It is found that all Type-C to Type-E OTPSM strategies can be obtained as particular solutions of (14).

Equivalently, from the viewpoint of volt-second balance, the magnetic fluxes of the series inductor L and magnetizing inductance L_m must be reset during transient state, such that the average values of the voltages across both L and L_m must be zero. By using superposition principle, the algebraic sums of the volt-second products caused by v_{ab} (in the time interval from t_0 to t_9) and v_{cd} (in the time interval from t_1 to t_{10}) should be individually equal to zero, that is

$$\begin{cases} V_1 T_{hc} - V_1 W_1 T_{hc} + V_1 W_2 T_{hc} - V_1 W_3 T_{hc} = 0 \\ N V_2 T_{hc} - N V_2 W_4 T_{hc} + N V_5 W_2 T_{hc} - N V_2 W_6 T_{hc} = 0. \end{cases} \tag{15}$$

Simplifying (15) and combining the result with (5) also leads to (14), which verifies that the fundamental principle of OTPSM is to establish a dynamic volt-second balance. However, as can be observed from Fig. 4, even if a dynamic volt-second balance of both L and L_m is achieved under Type-C to Type-E OTPSM strategies, transient dc offsets still exist in i_L and i_M. This suggests that the dynamic volt-second balance is only a partial, i.e., necessary but not sufficient, condition required for eliminating transient dc offsets in both i_L and i_M. This condition can only guarantee that i_L and i_M will enter into their new steady states from t_9, i.e., within one cycle, but it cannot guarantee that their dc offsets during transient state are zero.

B. Complete Elimination of Transient DC Offsets

As the previous studies of OTPSM only focused on achieving dynamic volt-second balance, they have failed to completely eliminate transient dc offsets. According to (1) and (2), if the average values of i_{ab} and i_{cd} are zero during transient state (i.e., the transient waveforms of i_{ab} and i_{cd} are symmetrical about the time axis), no dc offsets will be produced in both i_L and i_M, which, in fact, is a necessary and sufficient condition for

eliminating all transient dc offsets. More specifically, the integral values of i_{ab} and i_{cd} over the transient period should be zero. In other words, those shaded areas in Fig. 5 are required to satisfy

$$\begin{cases} S_{ab1} = S_{ab4} = S_{ab5} \\ S_{ab2} = S_{ab3} \\ S_{cd1} = S_{cd4} = S_{cd5} \\ S_{cd2} = S_{cd3} \end{cases} . \tag{16}$$

Solving (16) gives

$$\begin{cases} W_1 = W_3 \\ W_4 = W_6. \end{cases} \tag{17}$$

Combining (14) and (17) gives a more general and universal solution (18) that guarantees the elimination of dc offsets in both i_L and i_M during transient state

$$\begin{cases} W_1 = W_3 = (1 + W_2)/2 \\ W_4 = W_6 = (1 + W_5)/2 \\ 2W_2 + d = 2W_5 \end{cases} . \tag{18}$$

Although it is possible to derive various OTPSM strategies from (18), single-sided modulation is typically more attractive to engineers in practice due to simplicity, ease of implementation, and low hardware cost. When the pulse width of either v_{ab} or v_{cd} is set to a constant value of T_{hc}, there exist two simple particular solutions of (18), namely the following.

Type-I SS-OTPSM (v_{cd} is unmodulated)

$$\begin{cases} W_1 = W_3 = 1 - \frac{d}{4} \\ W_2 = 1 - \frac{d}{2} \\ W_4 = W_5 = W_6 = 1. \end{cases} \tag{19}$$

Type-II SS-OTPSM (v_{ab} is unmodulated)

$$\begin{cases} W_1 = W_2 = W_3 = 1 \\ W_4 = W_6 = 1 + \frac{d}{4} \\ W_5 = 1 + \frac{d}{2}. \end{cases} \tag{20}$$

From (19) and (20), SS-OTPSM is independent of any converter parameters and requires only the phase-shift increment or decrement d, which is directly available from the controller; hence, it requires no external sensing, i.e., being a sensorless solution, and can be implemented at low cost and low hardware complexity. When substituting $d = 0$ into (19) and (20), $W_1 - W_6$ become 1, and hence, SS-OTPSM is naturally compatible with conventional SPS modulation at steady state. It should be noted that, although the mathematical derivations of (19) and (20) are presented for the case of power increment ($d > 0$), i.e., increase in phase-shift ratio, the same equations are applicable to the case of power decrement ($d < 0$), i.e., decrease in phase-shift ratio. In addition, both Type-I and Type-II SS-OTPSM strategies do not distinguish between two power flow directions, and hence, (19) and (20) are applicable to all cases of power flow conditions and each case will be simply treated as a case of increasing/decreasing power (or phase-shift ratio).
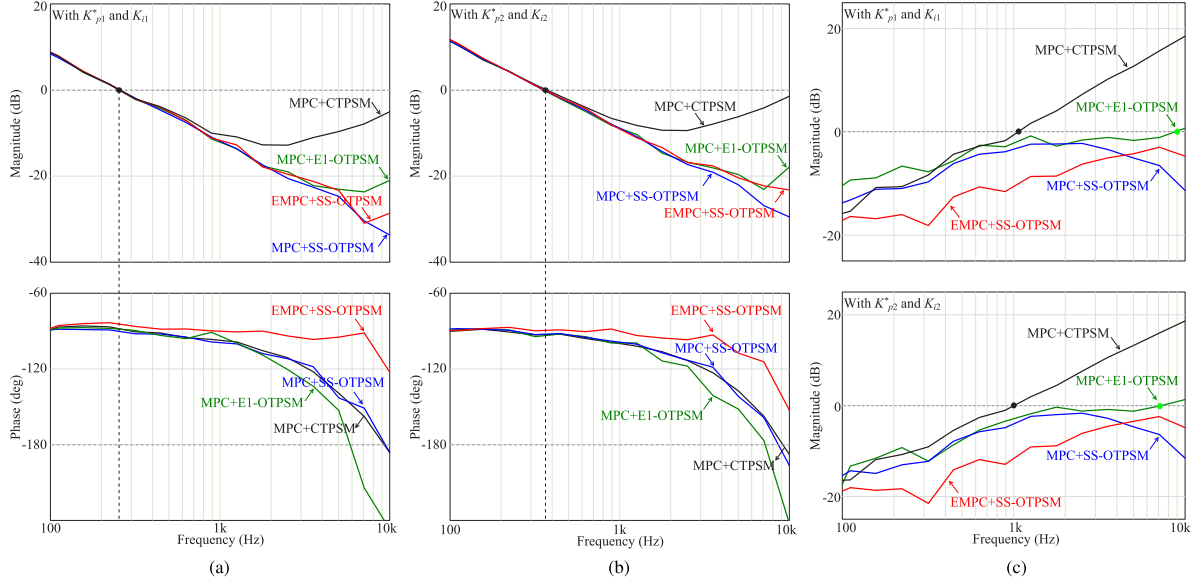
Fig. 10. Simulated loop gains and closed-loop output impedances under different systems. (a) Loop gains with K_{p1}^* and K_{i1}. (b) Loop gains with K_{p2}^* and K_{i2}. (c) Closed-loop output impedances.
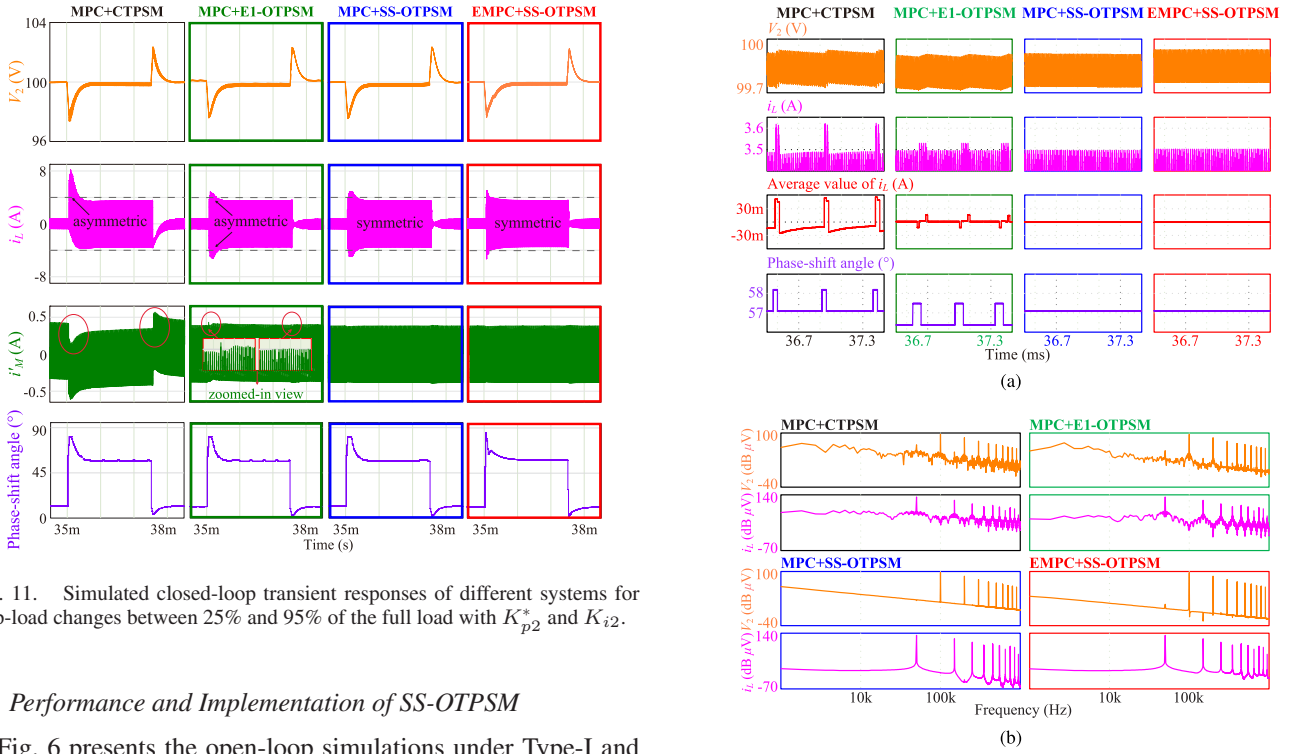

Fig. 11. Simulated closed-loop transient responses of different systems for step-load changes between 25% and 95% of the full load with K_{p2}^* and K_{i2}.

Fig. 12. Simulated steady-state waveforms under heavy-load condition with K_{p2}^* and K_{i2}. (a) Zoomed in steady-state waveforms of V_2, i_L, average value of i_L, and phase-shift angle. (b) FFT spectrum analysis of V_2 and i_L.

C. Performance and Implementation of SS-OTPSM

Fig. 6 presents the open-loop simulations under Type-I and Type-II SS-OTPSM strategies. Compared to the results presented in Figs. 3 and 4, the transient waveforms of i_L and i_M under both SS-OTPSM strategies show better symmetry due to the complete elimination of all transient dc offsets. By zooming out the transient waveforms, as shown in Fig. 6(b), the transient peaks are significantly reduced. However, two small but detectable transient peaks can be observed in i_M in Fig. 6(c), although the overall waveform remains symmetrical as a result of the elimination of transient dc offsets. It can be analyzed from (1) and (2) that i_{ab} and i_{cd} are equally important in determining i_L ($L_m \gg L_p$), while i_{cd} plays a more significant role in i_M since

the secondary-side leakage inductance L_s can be neglected in most practical applications of DABC. Therefore, any changes in v_{cd} can lead to overshoots/undershoots and noticeable transient waveform changes in i_M, as shown in Figs. 4 and 6(c). This observation reflects that (19), i.e., Type-I SS-OTPSM, which shows no such transient peaks [see Fig. 6(a)] is deemed more attractive for practical applications. For this reason, Type-I SS-OTPSM

is selected as the default modulation scheme in the following discussion of SS-OTPSM.

The performances of various OTPSM strategies are compared in Fig. 7 in a normalized form. The normalized percentages of improvement of different OTPSM strategies are obtained by computing the relative improvements with respect to CTPSM, where the data are summarized from Figs. 3, 4, and 6. The abbreviations for the performance measurements are defined as follows.

PM1 The maximum overshoot (or undershoot) of the positive (or negative) peak amplitude of the transient waveform of i_L.

PM2 The absolute value of the dc offset (or average value) of i_L over the first transient cycle for open-loop tests, or the first five transient cycles for closed-loop tests.

PM3 The maximum overshoot (or undershoot) of the positive (or negative) peak amplitude of the transient waveform of i'_M.

PM4 The absolute value of the dc offset (or average value) of i'_M over the first transient cycle for open-loop tests, or the first five transient cycles for closed-loop tests.

It can be seen that Type-I SS-OTPSM performs the best in all four key aspects. The main features of different OTPSM strategies are summarized and listed in Table I. It can be verified that all types of modulation strategies except Type-F OTPSM can be formulated by using (12) and (5), while Type-C to Type-E OTPSM and SS-OTPSM strategies can also be formulated by using (14). The expressions for the SS-OTPSM strategies, i.e., (19), and (20), can be regarded as the optimum solutions of (14).

In addition to poorer performances as shown in Fig. 7, one major problem with the existing OTPSM strategies is their high implementation complexity. Due to their asymmetric modulation characteristics, it is difficult for the existing OTPSM strategies to synchronize their phase-shifted PWM carriers in a cycle-by-cycle manner, and little information is disclosed regarding their implementation in closed-loop configuration. Fig. 8 illustrates the implementation of the proposed Type-I SS-OTPSM in the PWM modules of microprocessor. v_{ab} and v_{cd} are generated by employing two triangular carriers, where Carrier 2 and Carrier 1 correspond to the master and slave PWM modules, respectively. When an interrupt event occurs, the phase-shift ratio between v_{ab} and v_{cd} should be updated to $D+0.5d$, and the $(n+1)$th period of v_{ab} should be updated to $(2-d)T_{\text{hc}}$. Redefining the transient response time T_t as $T_t = (2-d)T_{\text{hc}}$, the duty-cycle values of v_{ab} will always be fixed at $W_2 T_{\text{hc}}/T_t = 0.5$, which ultimately makes it possible to change the pulse widths by only manipulating the PWM base frequency. With a constant duty ratio, triangle Carrier 1 has equal rise and fall times, and the resulting PWM waveform can be centered within each cycle.

In SS-OTPSM, the position of the sampling point can always be set at the mid-point of Carrier 1, such that the sampling and switching processes can be suitably synchronized. Synchronization allows the average sampled value to be exactly reconstructed and are robust against phase-shift variations and switching noise. In contrast to this, the sampling point under other asymmetric modulation strategies are rarely located at a
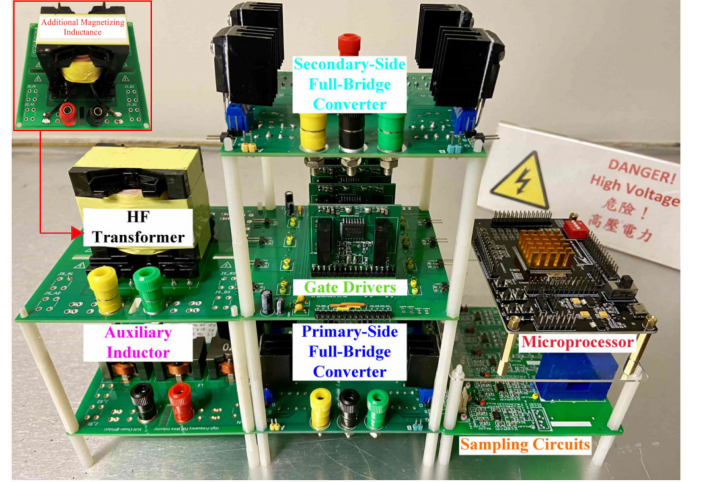

Fig. 13.   Photograph of the experimental DABC prototype.

fixed position (e.g., the beginning or middle point) with respect to each modulation period, and hence, the sampling signal is not perfectly synchronized with the carrier, resulting in aliasing effect and quantization noise in digitally controlled DABC, especially when the sampling rate is chosen to be close to the switching frequency [35]. The aliasing-induced error between the dc component of the sampled value and the actual dc voltage/current may be nonnegligible, thus degrading the closed-loop regulation accuracy and performance during both steady and transient states. By taking advantage of the symmetrical characteristic of the proposed SS-OTPSM, it is easy to reset the carriers after each execution, and achieve the synchronization between the sampling modules and PWM modules, which facilitates the continuous execution of SS-OTPSM in a closed-loop manner. This is a clear advantage of the proposed method over all existing ones.

V. Proposed Enhanced MPC for SS-OTPSM Modulated DABC

To evaluate the impact of SS-OTPSM on the dynamic performance of DABC under closed-loop configuration, a high-gain, fast MPC is used instead of the low-gain pure PI controller in [16]. This is because a PI controller cannot provide large step changes in phase-shift ratio and will result in a slow transient response and a large output voltage deviation. In such a case, no significant transient dc offsets will be introduced even by using CTPSM, and it is not possible to benefit from the superior transient performances of SS-OTPSM or OTPSM over CTPSM.

A. Conventional MPC

Although different MPCs have been developed for DABC, they can be generally depicted by the common block diagram in Fig. 9. V_{2_Ref} is the reference output voltage. $V_{1\_S}[n]$, $V_{2\_S}[n]$, and $I_{o\_S}[n]$ are the sampled values at the nth cycle, and they are used for generating the predicted output voltage $V_{2\_P}[n+1]$ according to a predictive model. $V_{2\_C}[n+1]$ is the corrected
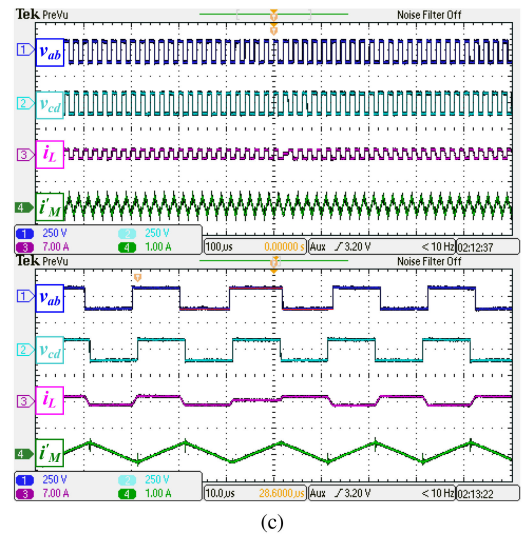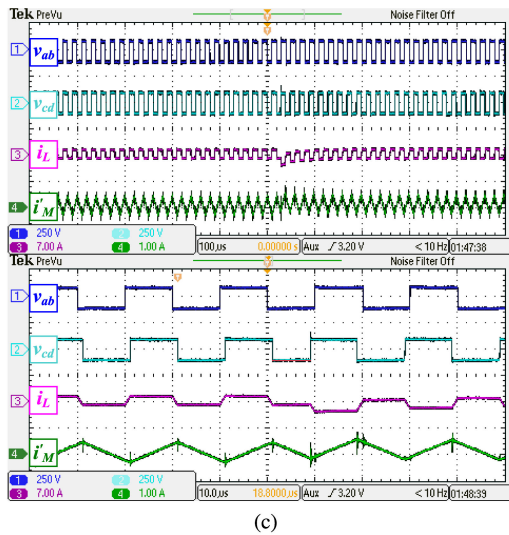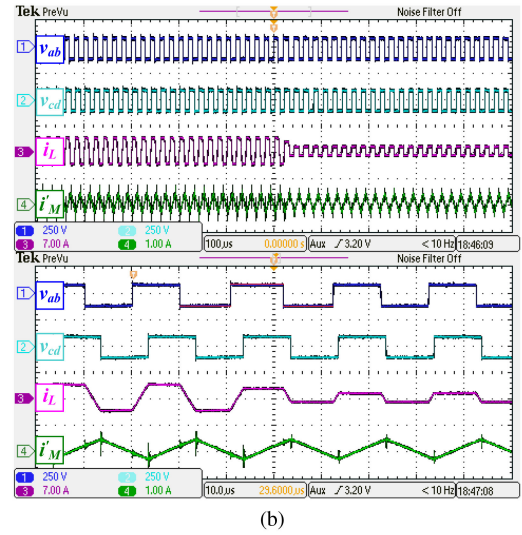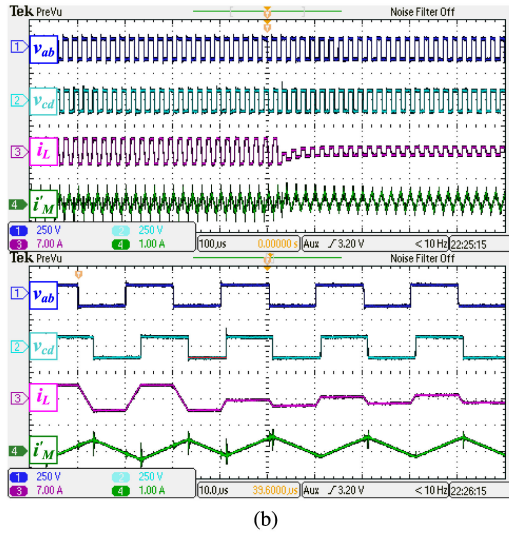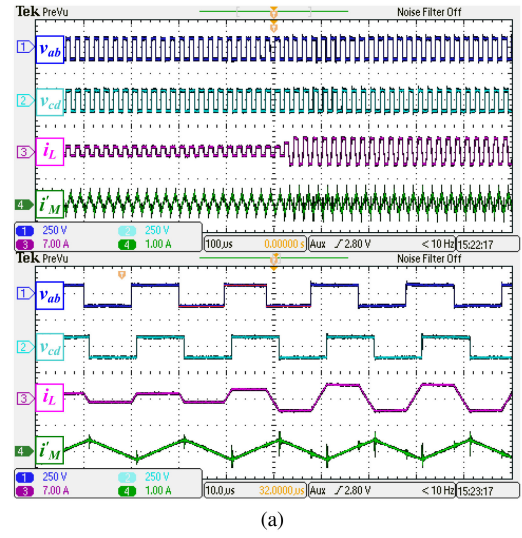
Fig. 14. Open-loop experimental results under CTPSM. (a) Phase-shift ratio is changed from $\frac{1}{9}$ to $\frac{1}{3}$. (b) Phase-shift ratio is changed from $\frac{1}{3}$ to $\frac{1}{9}$. (c) Phase-shift ratio is changed from $\frac{1}{9}$ to $-\frac{1}{9}$.

Fig. 15. Open-loop experimental results under the proposed SS-OTPSM. (a) Phase-shift ratio is changed from $\frac{1}{9}$ to $\frac{1}{3}$. (b) Phase-shift ratio is changed from $\frac{1}{3}$ to $\frac{1}{9}$. (c) Phase-shift ratio is changed from $\frac{1}{9}$ to $-\frac{1}{9}$.
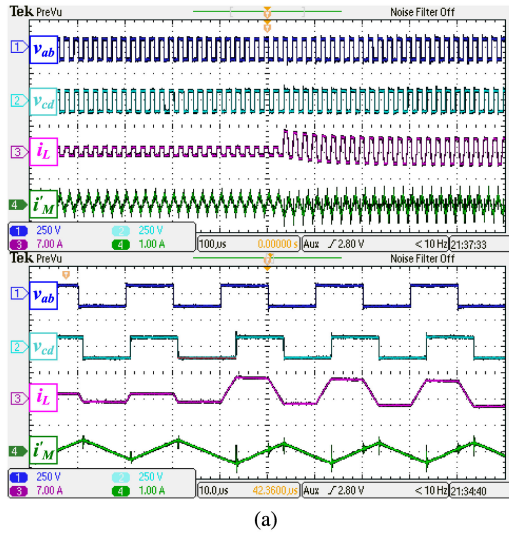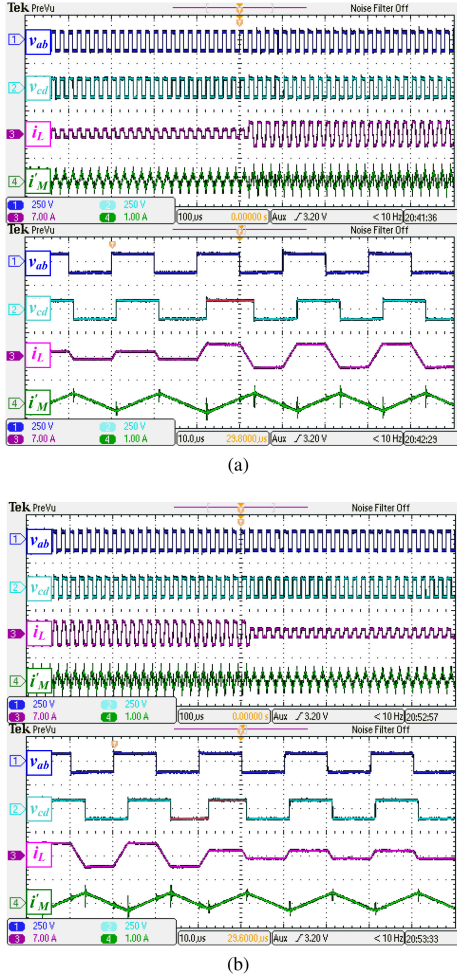
Fig. 16. Open-loop experimental results under Type-C_1 OTPSM [13]. (a) Phase-shift ratio is changed from $\frac{1}{9}$ to $\frac{1}{3}$. (b) Phase-shift ratio is changed from $\frac{1}{3}$ to $\frac{1}{9}$.

value of the output voltage after real-time error compensation. A given cost function J basically compares $V_{2\_C}[n+1]$ with V_{2_Ref} for calculating an optimal phase-shift ratio $D[n+1]$ for the next cycle that minimizes J. The major differences between the existing MPC schemes lie in their error compensators and cost functions. For example, in [2], a two-step prediction with a proportional compensator and a weighted cost function is implemented, while a one-step prediction using a PI compensator and a simple quadratic cost function are presented in [25]. To reduce computational burden, this article uses a simple scheme similar to that in [25].

Typically, the average value of i_2 (i.e., $\bar{i}_2$) can be predicted by the average power model of DABC [2] and is approximated by

$$\bar{i}_2 = \frac{P}{V_2} = \frac{NV_1 T_{hc} D(1-D)}{L}. \tag{21}$$

Hence, the dynamic behavior of V_2 is described by

$$C_o \frac{dV_2}{dt} = \bar{i}_2 - I_o = \frac{NV_1 T_{hc} D(1-D)}{L} - I_o. \tag{22}$$

The predicted output voltage at the $(n+1)$th cycle, i.e., $V_{2\_P}[n+1]$, can be obtained by discretizing (22) using the forward Euler

approximation, which leads to

$$V_{2\_P}[n+1] \approx V_{2\_S}[n] + 2T_{hc}V_2{}'[n]$$

$$= V_{2\_S}[n] + \frac{2NT_{hc}^2 D(1-D)V_{1\_S}[n]}{LC_o}$$

$$- \frac{2T_{hc}I_{o\_S}[n]}{C_o}. \tag{23}$$

In this article, the cost function J is defined as

$$J = [V_{2\_Ref} - V_{2\_C}[n+1]]^2 \tag{24}$$

and the PI-based error compensator is given by (25)

$$K_p V_{2\_E}[n] + K_i \sum_{\tau=0}^{n} V_{2\_E}[\tau] \tag{25}$$

where $V_{2\_E}[n] = V_{2\_Ref} - V_{2\_S}[n]$ is the output voltage error, and $V_{2\_C}[n+1] = V_{2\_P}[n+1] - (K_p V_{2\_E}[n] + K_i \sum_{\tau=0}^{n} V_{2\_E}[\tau])$. Minimizing J yields the optimal phase-shift ratio

$$D[n+1] = \frac{1}{2}\left(1 - \sqrt{1 - \frac{4K_2}{K_1}}\right) \tag{26}$$

where

$$K_1 = \frac{2NT_{hc}^2 V_{1\_S}[n]}{LC_o} \tag{27}$$

$$K_2 = 2T_{hc}I_{o\_S}[n]/C_o + K_p^* V_{2\_E}[n] + K_i \sum_{\tau=0}^{n} V_{2\_E}[\tau] \tag{28}$$

and

$$K_p^* = K_p + 1. \tag{29}$$

Equations (28) and (29) indicate that the presented controller attempts to correct the output voltage error V_{2_E} by an equivalent proportional gain K_p^* instead of K_p. Specifically, K_p^* determines the bandwidth of the control loop, suppresses sampling noise, and stabilizes the converter; while the integral gain K_i is used for eliminating steady-state tracking error.

B. Proposed EMPC Based on SS-OTPSM

A major problem with the abovementioned predictive model is that the average power computed from (4) is derived based on steady-state waveforms. Hence, it cannot accurately predict the average power transferred to the load during transient period. Especially when a large step change in load occurs, the phase-shift ratio predicted by conventional model typically tends to deviate from the actual desired value, thus resulting in modeling error and longer transient response time. Hence, a refined model is required to describe the cycle-to-cycle dynamic properties of DABC. However, since the initial/final value of i_L in each transient cycle is uncertain depending on many factors such as R_s, the transient average power under CTPSM is difficult to predict. This problem can be easily overcome by the proposed SS-OTPSM. Since the inductor current can be modulated to the desired value during each cycle, the average power of DABC operating under SS-OTPSM can be correctly predicted and

Symbol	Parameter description	Value or part type
$P_{\max}$	Rated power	250 W
V_1	Input voltage	100 V
V_2	Output voltage	100 V
C_o	Output capacitance	47 μF
R_L	Load resistance	150/43 Ω
$N:1$	Transformer ratio	1 : 1
L_m	Magnetizing inductance	650 μH
R_m	ESR of L_m	260 mΩ
L_p	Primary inductance	92 μH
R_p	ESR of L_p	211 mΩ
L_s	Secondary inductance	1.7 μH
$S_x - Q_x$	Power switches	UnitedSiC UJC06505K
f_s	Switching frequency	50 kHz
–	Dead time	250 ns
–	Voltage sensing circuit	Resistive voltage divider
–	Current sensor	LEM LA 55-P
–	Microprocessor	TI TMS320F28335

modeled cycle by cycle. If so, the predicted control variable (or phase-shift ratio) will be exactly proportional to the transferred power, and there is neither steady-state nor transient modeling error between them. To achieve this, an EMPC as presented in the following that is compatible with SS-OTPSM is proposed in this article.

By referring to Fig. 8, the average power under SS-OTPSM over the $(n+1)$th cycle is given by

$$
\begin{aligned}
P^* &= \frac{1}{(2-d)T_{\mathrm{hc}}} \int_0^{(2-d)T_{\mathrm{hc}}} v_{ab}(t)i_L(t)\mathrm{d}t \\
&= \frac{NV_1V_2T_{\mathrm{hc}}(8d - 9d^2 + 16D - 24Dd - 16D^2)}{4(2-d)L}
\end{aligned} \tag{30}
$$

which can be used to accurately predict the transient output power under SS-OTPSM. To compute the optimal phase-shift ratio, (31) gives the dynamic output voltage in continuous-time

$$
C_o \frac{\mathrm{d}V_2}{\mathrm{d}t} = \bar{i}_2 - I_o = \frac{P^*}{V_2} - I_o. \tag{31}
$$

Discretizing (31) with forward Euler method, the output voltage under SS-OTPSM can be predicted using (32)

$$
V_{2\_P}^*[n+1] \approx V_{2\_S}[n] + 2T_{\mathrm{hc}}\left(\frac{P^*}{C_oV_2} - \frac{I_{o\_S}[n]}{C_o}\right). \tag{32}
$$

Substituting (32) into (24) and minimizing J, it can be shown that the refined optimal phase-shift ratio $D^*[n+1]$ employing EMPC is given by

$$
\begin{aligned}
D^*[n+1] &= D[n] + d^* = \frac{(4 - 3D[n])K_1 + 2K_2}{9K_1} \\
&- \frac{2\sqrt{4(1 + 3D[n])K_1^2 - 2(7 + 6D[n])K_1K_2 + K_2^2}}{9K_1}. \tag{33}
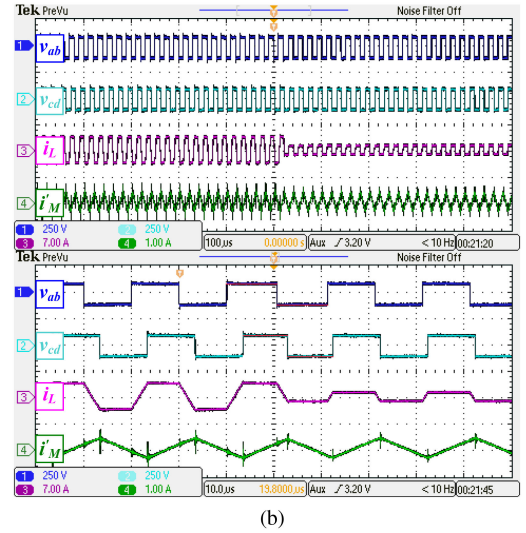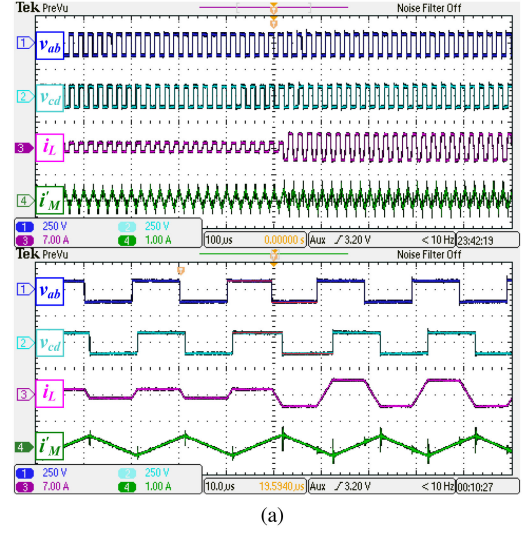\end{aligned}
$$

Fig. 17. Open-loop experimental results under Type-E_1 OTPSM [16]. (a) Phase-shift ratio is changed from $\frac{1}{9}$ to $\frac{1}{3}$. (b) Phase-shift ratio is changed from $\frac{1}{3}$ to $\frac{1}{9}$.

Hence, compared to (26), a more accurate prediction of the optimal phase-shift ratio is given by (33).

Compared to conventional MPC, EMPC results in a more accurate prediction of the optimal phase-shift ratio, which is to be executed by SS-OTPSM. Otherwise, in the presence of significant error in the predicted optimal phase-shift ratio by conventional MPC, the performance merits of SS-OTPSM will also be adversely affected. This highlights the importance of co-optimization of controller and transient modulation designs in order to achieve a truly optimal dynamic performance.

C. Closed-Loop Simulation Results of Different Systems

To compare the dynamic performances of different combinations of controllers and transient modulation strategies, four cases are selected, i.e., MPC+CTPSM, MPC+E_1-OTPSM, MPC+SS-OTPSM, and EMPC+SS-OTPSM, and two sets of K_p^*
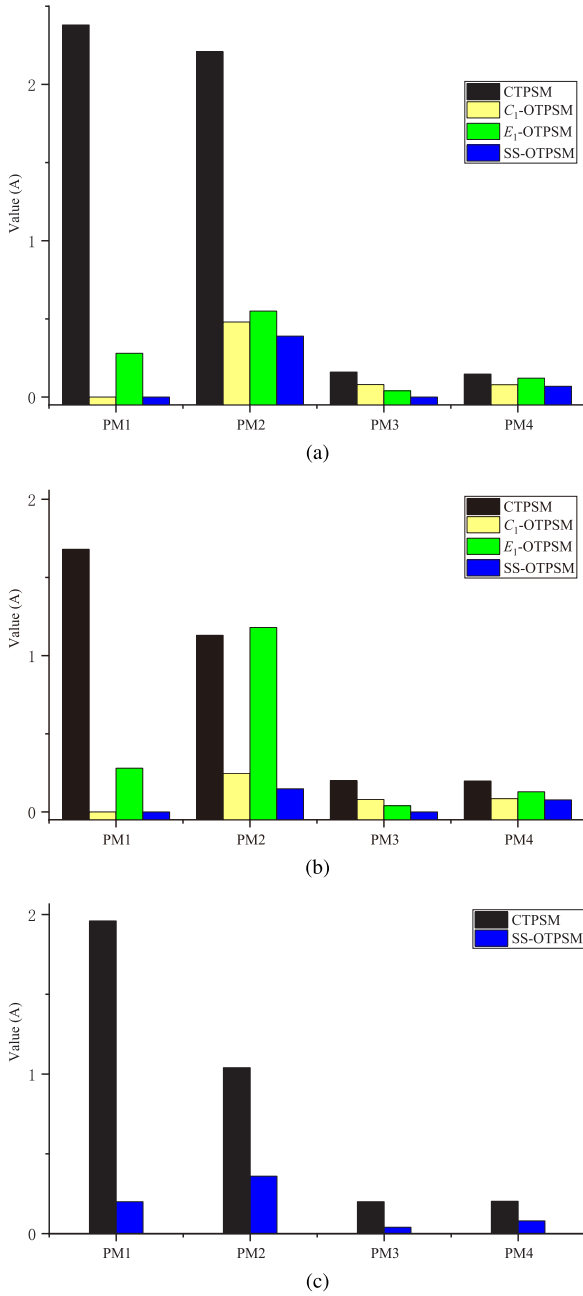
Fig. 18. Performance evaluation of different transient modulation strategies in open-loop experiments. (a) For an increase in the phase-shift ratio from $\frac{1}{9}$ to $\frac{1}{3}$. (b) For an decrease in the phase-shift ratio from $\frac{1}{3}$ to $\frac{1}{9}$. (c) Phase-shift ratio is changed from $\frac{1}{9}$ to $-\frac{1}{9}$.

and K_i values are chosen according to the system requirements, i.e., $\{K_{p1}^* = 0.07, K_{i1} = 0.3\}$ and $\{K_{p2}^* = 0.1, K_{i2} = 0.5\}$.

Fig. 10(a) and (b) shows the simulated loop gain, i.e., open-loop transfer function from $\hat{V}_{2\_E}(s)$ to $\hat{V}_2(s)$, with the two sets of control parameters, respectively. It can be seen that the system responses of the four cases are similar in the low-frequency region, and the difference mainly lies in the high-frequency region. Although the crossover frequencies and phase margin values of the four different systems are similar, SS-OTPSM is observed to possess a higher disturbance attenuation capability

than CTPSM and E_1-OTPSM since the magnitude responses of MPC+SS-OTPSM and EMPC+SS-OTPSM decrease monotonically in the high-frequency region. Therefore, for similar phase margins, both MPC+SS-OTPSM and EMPC+SS-OTPSM exhibit significantly larger gain margins compared to the other two systems. As shown by the Bode plots, in the high-frequency region, the system's magnitude response under MPC+CTPSM is significantly higher than those of the other systems, and the system's phase response under MPC+E_1-OTPSM lags those of the other systems and becomes $-180°$ at a relatively low frequency, which makes them prone to stability problem. In summary, with the same control coefficients, the closed-loop controlled DABC is expected to exhibit better stability and transient performances under MPC+SS-OTPSM and EMPC+SS-OTPSM.

In addition, the closed-loop output impedances of different systems are simulated by PSIM and shown in Fig. 10(c). It can be seen that the output impedance of the MPC+CTPSM system reaches 0 dB at about 1 kHz; the output impedance of the MPC+E_1-OTPSM system reaches 0 dB at 8.7 kHz with K_{p1}^* and K_{i1} and about 7 kHz with K_{p2}^* and K_{i2}; while the output impedances of both MPC+SS-OTPSM and EMPC+SS-OTPSM systems remain below 0dB over a wide-frequency range from 100 Hz to 10 kHz. MPC+E_1-OTPSM always exhibits a higher output impedance than MPC+SS-OTPSM and EMPC+SS-OTPSM. Compared with MPC+CTPSM and MPC+E_1-OTPSM, both MPC+SS-OTPSM and EMPC+SS-OTPSM are able to achieve a lower closed-loop output impedance, better stability, and hence, a better disturbance-rejection performance when subjected to large step-load changes.

As exemplified in Fig. 11, it is evident from the simulated closed-loop transient responses that the dc offsets arising from CTPSM are largely mitigated by E_1-OTPSM and SS-OTPSM, but the transient waveforms of i_L and i'_M under MPC+E_1-OTPSM still exhibit some noticeable asymmetry compared to SS-OTPSM. With the same control parameter values, EMPC+SS-OTPSM demonstrates the fastest transient response with zero dc offsets in both i_L and i'_M, although its transient overshoots and undershoots are slightly higher than those under MPC+SS-OTPSM.

Furthermore, by zooming in the steady-state waveforms of V_2 and i_L of different systems under heavy-load condition, another interesting finding is that limit-cycle oscillations are observed under both MPC+CTPSM and MPC+E_1-OTPSM in steady state, while such oscillations are not observed under both MPC+SS-OTPSM and EMPC+SS-OTPSM. To illustrate this phenomenon, Fig. 12(a) shows the zoomed-in simulated steady-state waveforms with control parameters K_{p2}^* and K_{i2}. Although the integral term in the feedback loop can significantly eliminate steady-state error and help us to reduce the amplitudes of limit-cycle oscillations to an acceptable level, such oscillations cannot be effectively attenuated if their frequencies are beyond the controller's bandwidth. Typically, the amplitude and frequency of limit-cycle oscillations depend strongly on the nonlinear quantization effects caused by the interaction between the resolutions of PWM generator and sampling module [35]. According to the fast Fourier transform (FFT)
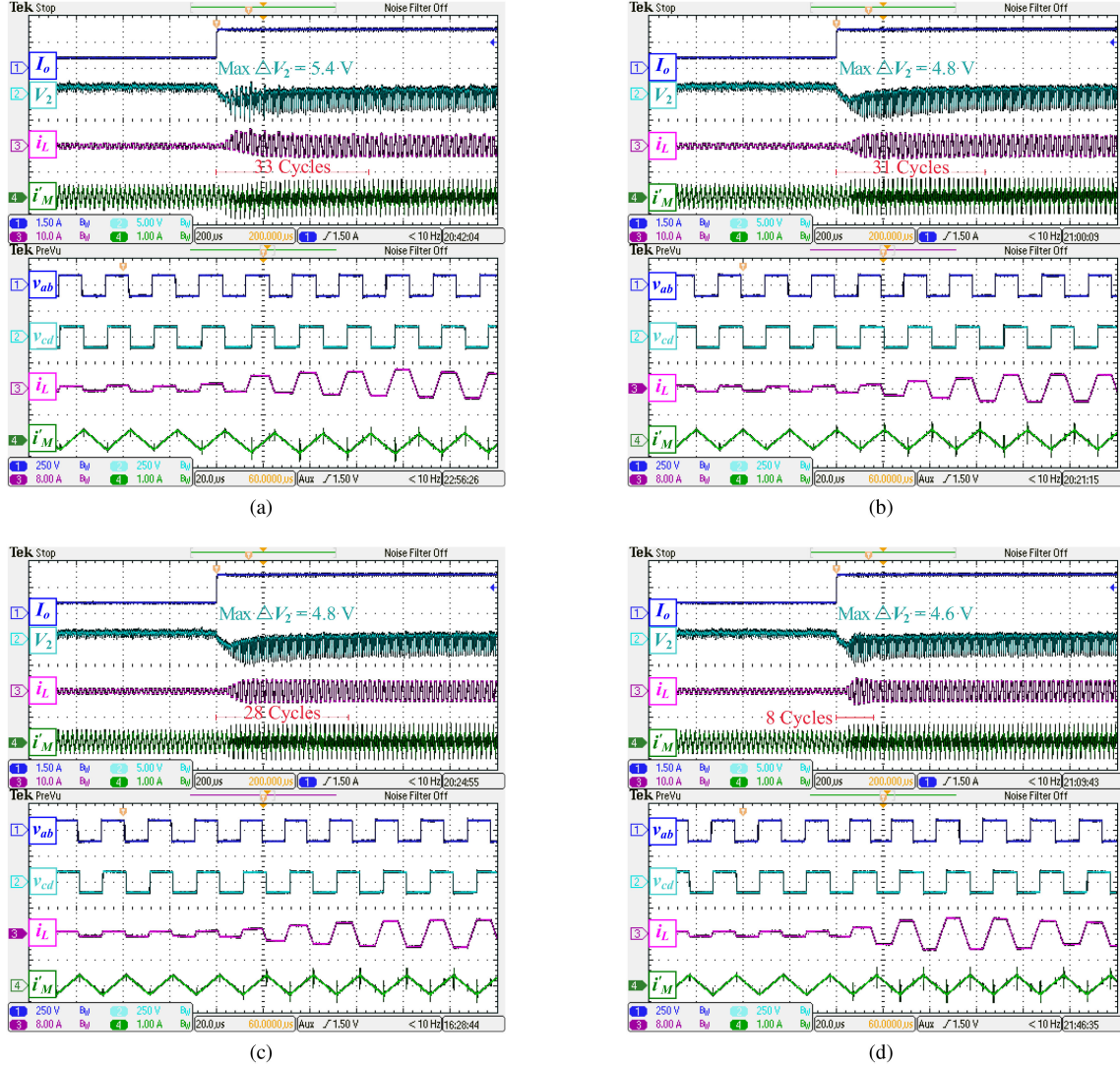
Fig. 19.   Experimental closed-loop transient responses for a step change in the load from 25% to 95% with $\{K_{p1}^* = 0.07, K_{i1} = 0.3\}$ under (a) MPC+CTPSM, (b) MPC+E_1-OTPSM, (c) MPC+SS-OTPSM, and (d) EMPC+SS-OTPSM.

analysis of V_2 and i_L shown in Fig. 12(b), some switching noise and spectral aliasing can be found in the spectrums under MPC+CTPSM and MPC+E_1-OTPSM, which are not seen under MPC+SS-OTPSM and EMPC+SS-OTPSM as they can achieve synchronous sampling. The aliasing effect can affect the regulation precision of output voltage and further lead to permanent small-amplitude disturbances in the control variable (i.e., phase-shift angle). Moreover, since any changes in the control variable may give rise to dc offsets, which cannot be completely eliminated by CTPSM or even E_1-OTPSM, considerable steady-state error can accumulate in the control loop. As shown in Fig. 12(a), the average value of i_L periodically oscillates around zero under MPC+CTPSM and MPC+E_1-OTPSM, while it is within the zero-error bin under MPC+SS-OTPSM and EMPC+SS-OTPSM. As demonstrated by the simulation results, in addition to enhancing transient response, both MPC+SS-OTPSM and EMPC+SS-OTPSM can achieve more precise regulation and suppress limit-cycle oscillations

with the same control parameters since the aliasing effect can be neglected under SS-OTPSM. These abovementioned findings are evidences of the correctness of the theoretical analysis presented in the current and the last sections.

VI. EXPERIMENTAL RESULTS

In order to verify the advantages of the proposed SS-OTPSM and EMPC, both open-loop and closed-loop experiments are carried out on a scaled-down prototype as shown in Fig. 13 with the key specifications listed in Table II. In open-loop tests, both terminals of DABC are connected with dc voltage sources, and additional resistors are connected in parallel to each source such that the direction of the power flow can be reversed. The phase-shift ratio is changed directly by giving command through a human–machine interaction software. In closed-loop tests, the output terminal is connected to resistive loads instead of a dc-voltage source, and the load resistances can be switched by using
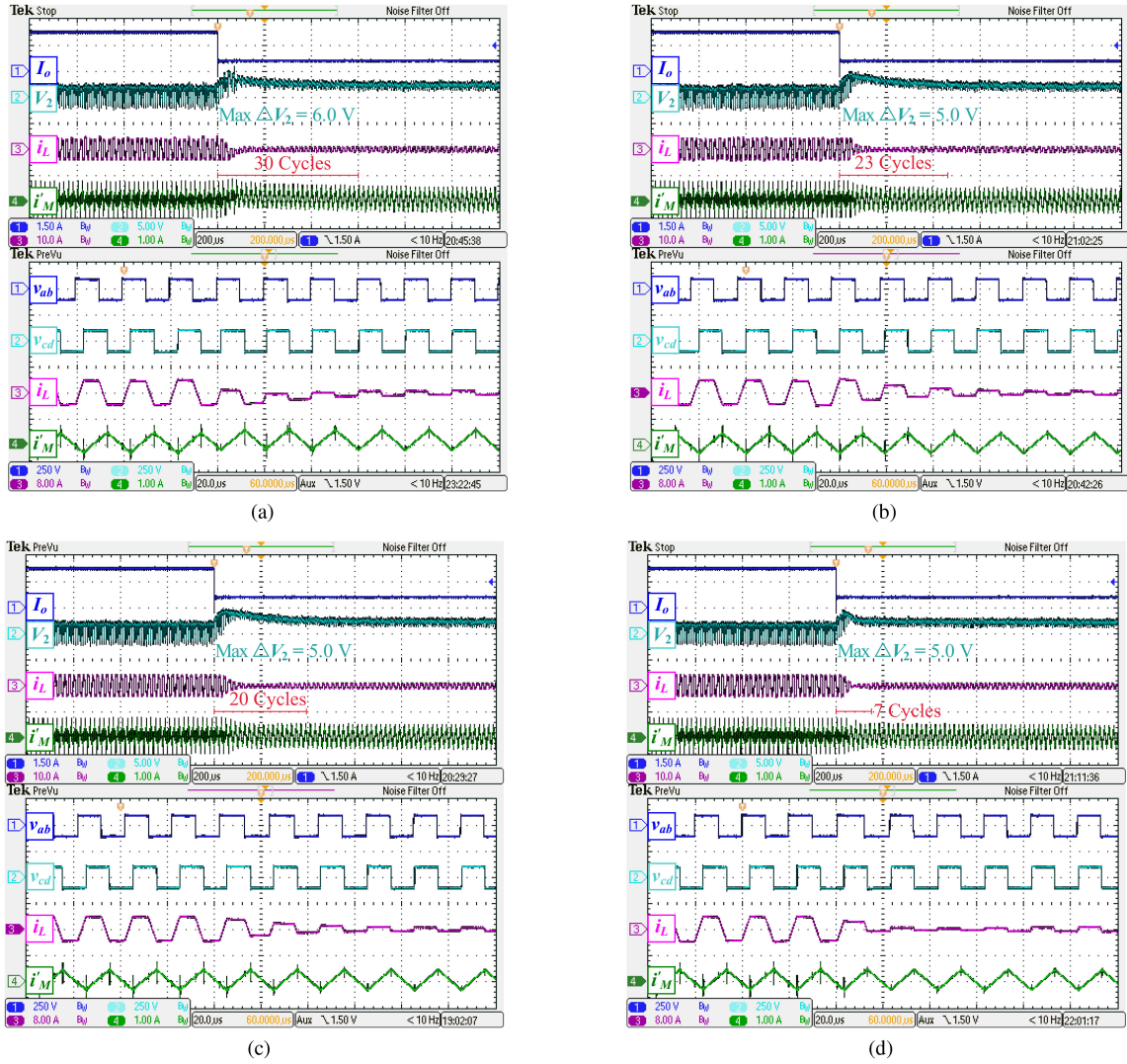
Fig. 20. Experimental closed-loop transient responses for a step change in the load from 95% to 25% with $\{K_{p1}^* = 0.07, K_{i1} = 0.3\}$ under (a) MPC+CTPSM, (b) MPC+E_1-OTPSM, (c) MPC+SS-OTPSM, and (d) EMPC+SS-OTPSM.

a power MOSFET. The MPC or EMPC designed in Section V will determine the desired phase-shift ratio based on the sampled information.

According to Fig. 7 and Table I, since Type-A, Type-B, Type-D, and Type-F OTPSM strategies do not show any significant advantages over other strategies, they will not be further discussed in this section. For performance comparisons, the two most-cited sensorless methods, i.e., Type-C_1 and Type-E_1 OTPSM strategies are implemented in open-loop experiments; Type-E_1 OTPSM is also implemented with a high-bandwidth MPC in closed-loop experiments as it is the only existing method that has been verified in closed-loop configuration, albeit with a low-bandwidth pure PI controller, which is not suitable for use with OTPSM or SS-OTPSM.

A. Open-Loop Tests

Figs. 14–17 show the open-loop experimental results under CTPSM, the proposed SS-OTPSM, Type-C_1 OTPSM [13], and

Type-E_1 OTPSM [16], respectively. Note that, by updating the phase-shift ratio from $1/9$ to $-1/9$, the direction of power flow reverses in Figs. 14(c) and 15(c), and the experimental results confirmed that SS-OTPSM can be applied in all power flow conditions.

Extracting the performance data of open-loop experiments from Figs. 14–17, the performance evaluations of different transient modulation strategies are presented in Fig. 18. It can be seen that when there are abrupt and large-amplitude changes in phase-shift ratio, SS-OTPSM and OTPSM have shown a number of advantages over CTPSM. Under CTPSM, the transient waveforms of i_L and i_M' take several cycles to reach their new steady states, but it takes only about one cycle under SS-OTPSM and OTPSM to achieve the same states. In addition, large peak overshoots/undershoots and excessive transient dc offsets in i_L and i_M' are eliminated under SS-OTPSM and OTPSM. As a result, the transient current stresses on the power devices are significantly reduced and the saturation of magnetic elements can be prevented.
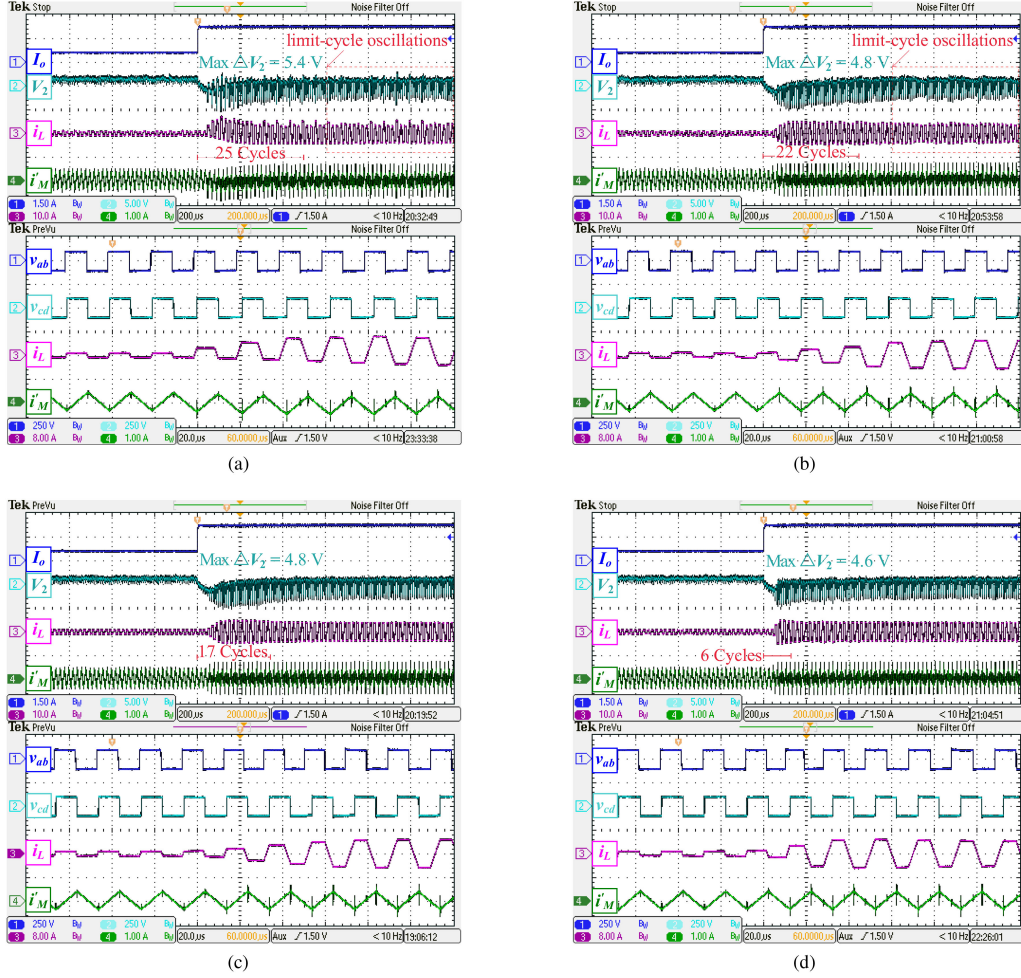
Fig. 21. Experimental closed-loop transient responses for a step change in the load from 25% to 95% with $\{K_{p2}^* = 0.1, K_{i2} = 0.5\}$ under (a) MPC+CTPSM, (b) MPC+E_1-OTPSM, (c) MPC+SS-OTPSM, and (d) EMPC+SS-OTPSM.

It is worth noting that, besides achieving a lower dc offset in i_L, the dc offset and overshoot (or undershoot) in i_M' under SS-OTPSM are found to be significantly lower than those achieved with both Type-C_1 and Type-E_1 OTPSM strategies, since the transient operations of these two OTPSM strategies involve waveform changes in v_{cd}. Essentially, the proposed SS-OTPSM is a member of the class of OTPSM strategies. However, according to the performance evaluation described in Fig. 18, SS-OTPSM performs better than the other two OTPSM strategies due to its capability in further suppressing transient dc offsets in both i_L and i_M simultaneously. This finding is consistent with the open-loop simulation results presented in Fig. 7 and the theoretical analysis of SS-OTPSM and OTPSM.

Compared with all the existing OTPSM strategies, SS-OTPSM is more readily implemented in a cycle-by-cycle manner in microprocessors due to its conceptual simplicity and lower implementation complexity, which makes it inherently suitable for practical use. In the following section, the performance of SS-OTPSM will be further examined by closed-loop experiments.

B. Closed-Loop Tests

To compare the closed-loop dynamic performances under MPC+CTPSM, MPC+E_1-OTPSM, MPC+SS-OTPSM, and EMPC+SS-OTPSM, experimental results of step-load changes between 25% and 95% of the full load are shown in Figs. 19–22, where the maximum output voltage deviation (i.e., Max ΔV_2) and settling time are annotated. The control parameters of $\{K_{p1}^* = 0.07, K_{i1} = 0.3\}$ are used for the tests shown in Figs. 19 and 20, and $\{K_{p2}^* = 0.1, K_{i2} = 0.5\}$, which correspond to a fast-loop configuration, are depicted in Figs. 21 and 22. It should be noted that the control parameters and experimental conditions used in the subfigures of Figs. 19–22 are identical. The performance data of these closed-loop experiments are extracted and compared in Fig. 23 in terms of PM1–PM4.

Generally, the experimental transient responses depicted in Figs. 19–22 match closely with the simulation results shown in Fig. 11. As expected, excessive overshoots (or undershoots) and transient dc offsets are observed in both i_L and i_M' under MPC+CTPSM, and these dc offsets have significant influences on the high-frequency-link waveforms, such as the ripples of
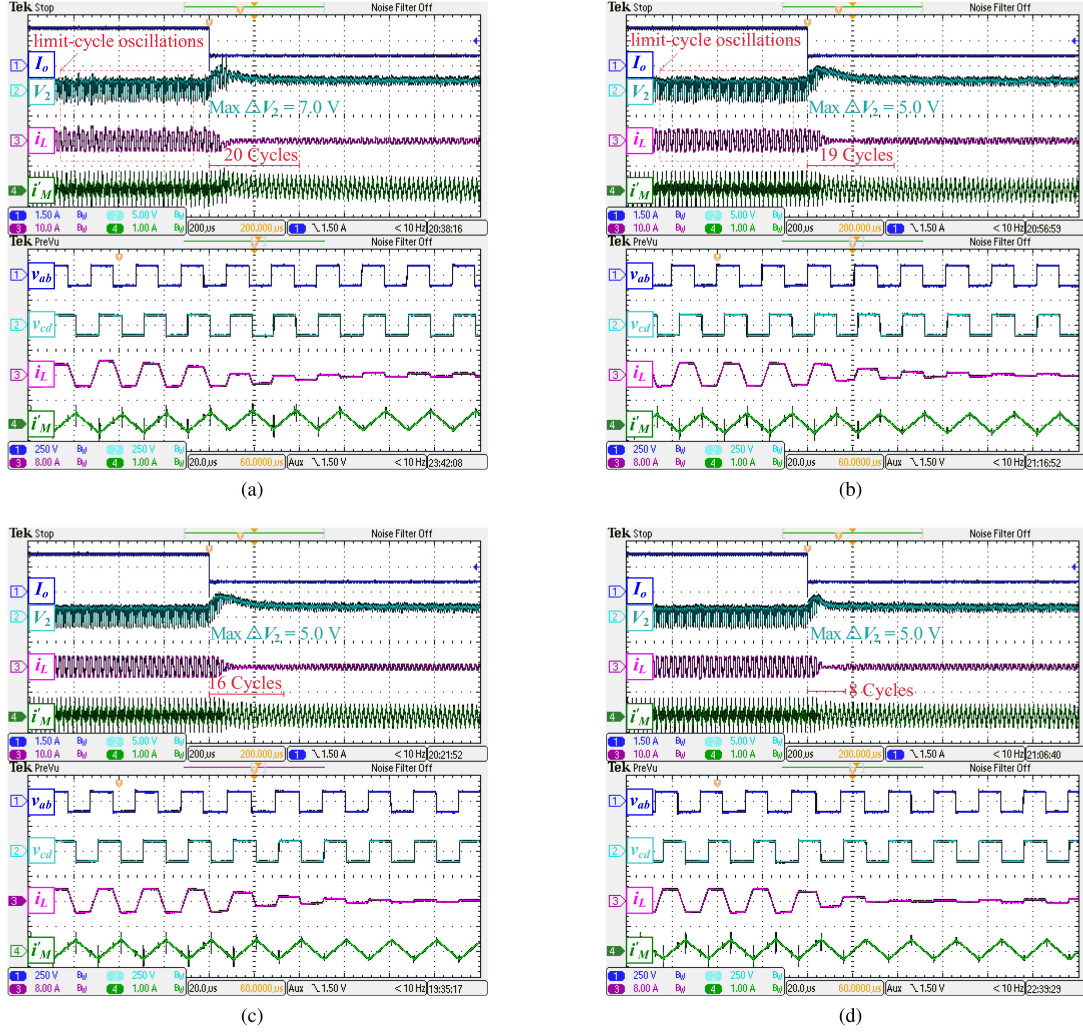
Fig. 22.   Experimental closed-loop transient responses for a step change in the load from 95% to 25% with $\{K_{p2}^* = 0.1,\ K_{i2} = 0.5\}$ under (a) MPC+CTPSM, (b) MPC+E_1-OTPSM, (c) MPC+SS-OTPSM, and (d) EMPC+SS-OTPSM.

V_2, which results in the largest output voltage deviation in all different cases. As shown in Figs. 21 and 22, these issues become even more apparent in the case of increased bandwidth, i.e., with K_{p2}^* and K_{i2}. In contrast to this, all such problems associated with transient dc offsets are largely suppressed under E_1-OTPSM and SS-OTPSM. According to Fig. 23, and the results of performance comparison suggest that MPC+SS-OTPSM outperforms MPC+CTPSM and MPC+E_1-OTPSM in the four key performance aspects, i.e., PM1–PM4. It is also observed that the settling times under MPC+CTPSM are always the longest compared to other systems, and the settling times under MPC+SS-OTPSM are always shorter than those under MPC+E_1-OTPSM. As a result, compared with the conventional scheme (i.e., MPC+CTPSM), both MPC+OTPSM and MPC+SS-OTPSM are effective in improving the dynamic performance of DABC, and MPC+SS-OTPSM is the most effective one as it can provide the fastest transient response, lowest transient dc offsets, and smallest overshoots/undershoots in all cases.

However, although transient dc offsets can be significantly reduced, the settling times achieved under both MPC+E_1-OTPSM and MPC+SS-OTPSM are only several cycles shorter than those achieved under MPC+CTPSM. As analysed in Section V-B and V-C, a refined EMPC that matches the transient operation of SS-OTPSM is required to fully realize its potential benefits. Referring to the experimental results shown in Figs. 19–22, under EMPC+SS-OTPSM, the settling times can be significantly reduced to 6–8 cycles with no obvious increase in the overshoot/undershoot of i_L and i_M', and the output voltage deviation is also the smallest compared with other systems, which verifies the positive contribution of the proposed EMPC in realizing the benefits of SS-OTPSM to the fullest without further modification of control parameters. In all cases, EMPC+SS-OTPSM minimizes the trajectory tracking error and optimizes the inductor current (as well as the magnetizing current) to ensure minimum transient response time and waveform distortions, thus enabling an optimal transient performance of an MPC-controlled DABC.
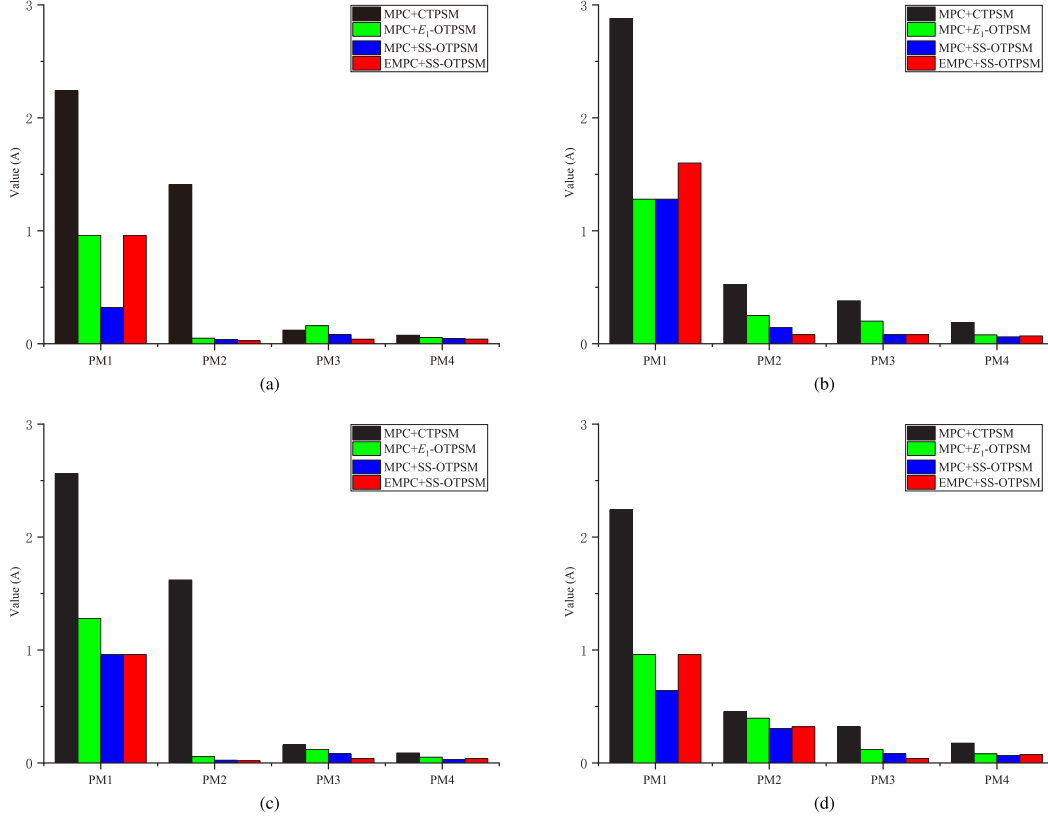
Fig. 23. Performance evaluation of closed-loop experiments. (a) Load step-up transition with $\{K_{p1}^* = 0.07, K_{i1} = 0.3\}$. (b) Load step-down transition with $\{K_{p1}^* = 0.07, K_{i1} = 0.3\}$. (c) Load step-up transition with $\{K_{p1}^* = 0.10, K_{i1} = 0.5\}$. (d) Load step-down transition with $\{K_{p1}^* = 0.10, K_{i1} = 0.5\}$.

In addition, as can be seen from Figs. 21(a), (b), 22(a), and (b), there are small-amplitude limit-cycle oscillations in the steady-state waveforms of V_2 and i_L under MPC+CTPSM and MPC+E_1-OTPSM, which are similar to the observations in Fig. 12(a). As explained previously, these low-frequency oscillations are caused by the presence of accumulated errors due to aliasing effect, and the presence of residual transient dc offsets. In general, an incompatible transient modulation tends to introduce switching noise, quantization noise, multiple time delays, etc., to the control loop, which ultimately results in reduced stability and, hence, degraded steady-state and transient performances in DABC. Since the volt-second product on the energy-transfer inductor and magnetizing inductor can be more precisely balanced under SS-OTPSM, it is more robust than CTPSM and E_1-OTPSM in terms of error compensation and control performance. Hence, a major advantage of SS-OTPSM is its ease of use and compatibility with high-bandwidth (or high-gain) controllers for achieving fast convergence to new steady states without oscillation when implemented in closed-loop configuration.

VII. CONCLUSION

This article comprehensively overviews the existing OTPSM strategies for SPS modulated DABC under a unified transient-modulation framework. The presented theoretical analysis reveals that satisfying dynamic volt-second balance alone does not guarantee the complete elimination of transient dc offsets in both energy-transfer and transformer's magnetizing inductors during transient state, unless the time-averaged values of i_{ab} and i_{cd} over the transient state are maintained at zero. A symmetric SS-OTPSM strategy is then proposed based on this theory. As confirmed by simulation and experimental results, the newly proposed SS-OTPSM demonstrates its superiority over CTPSM and other existing OTPSM strategies in its total elimination of the transient dc offsets in both energy-transfer and transformer's magnetizing inductors under all different open-loop operating conditions. It is by far the simplest and most effective OTPSM strategy unmatched by all existing OTPSM-based strategies.

This article also reveals the importance of controller design on the effectiveness of transient modulation. When conventional power calculation associated with steady-state operation is adopted for implementing MPC+SS-OTPSM, the significant error present in the power calculation has led to an erroneous prediction of the optimal phase-shift ratio, and hence, a suboptimal performance of SS-OTPSM similar to the performances of CTPSM and older OTPSM strategies. It has been successfully demonstrated that, through the use of an augmented power calculation matching the operation of SS-OTPSM and its application in an EMPC, a remarkable improvement in transient performance has been achieved where the settling time is reduced by over 50%. Overall, through the co-optimization of SS-OTPSM and EMPC, truly optimal dynamics of DABC can be achieved easily and cost effectively.

Our future research will focus on extending the proposed transient modulation scheme and co-optimization approach to closed-loop controlled, MPS and variable-frequency modulated DABC.

REFERENCES

[1] B. Zhao, Q. Song, W. Liu, and Y. Sun, "Overview of dual-active-bridge isolated bidirectional DC–DC converter for high-frequency-link power-conversion system," *IEEE Trans. Power Electron.*, vol. 29, no. 8, pp. 4091–4106, Aug. 2014.

[2] L. Chen, S. Shao, Q. Xiao, L. Tarisciotti, P. W. Wheeler, and T. Dragičević, "Model predictive control for dual-active-bridge converters supplying pulsed power loads in naval DC micro-grids," *IEEE Trans. Power Electron.*, vol. 35, no. 2, pp. 1957–1966, Feb. 2020.

[3] N. Hou and Y. W. Li, "Overview and comparison of modulation and control strategies for a nonresonant single-phase dual-active-bridge DC–DC converter," *IEEE Trans. Power Electron.*, vol. 35, no. 3, pp. 3148–3172, Mar. 2020.

[4] S. Shao *et al.*, "Modeling and advanced control of dual-active-bridge DC–DC converters: A review," *IEEE Trans. Power Electron.*, vol. 37, no. 2, pp. 1524–1547, Feb. 2022.

[5] B. Zhang, S. Shao, L. Chen, X. Wu, and J. Zhang, "Steady-state and transient DC magnetic flux bias suppression methods for a dual active bridge converter," *IEEE Trans. Emerg. Sel. Topics Power Electron.*, vol. 9, no. 1, pp. 744–753, Feb. 2021.

[6] X. Li and Y.-F. Li, "An optimized phase-shift modulation for fast transient response in a dual-active-bridge converter," *IEEE Trans. Power Electron.*, vol. 29, no. 6, pp. 2661–2665, Jun. 2014.

[7] C. Sun and X. Li, "Instantaneous current balance modulation for fast transient response in a dual-active-bridge converter," in *Proc. IEEE Int. Power Electron. Appl. Conf. Expo.*, 2018, pp. 1–6.

[8] R. Chattopadhyay, U. Raheja, G. Gohil, V. Nair, and S. Bhattacharya, "Sensorless phase shift control for phase shifted DC–DC converters for eliminating dc transients from transformer winding currents," in *Proc. IEEE Appl. Power Electron. Conf. Expo.*, 2018, pp. 1882–1889.

[9] J. Yin, J. Lu, Y. Liu, J. Peng, and H. Jiang, "Novel phase-shift method for fast power reversal with transient zero voltage switching in a bidirectional dual active bridge DC–DC converter," *IEEE Trans. Ind. Electron.*, vol. 68, no. 9, pp. 8028–8038, Sep. 2021.

[10] Y. Tang, X. Li, S.-Z. Zhou, C. Sun, and G. Chen, "Comprehensive study of fast load modulation with volt-second balance in a dual-active-bridge converter," *IET Power Electron.*, vol. 12, no. 6, pp. 1357–1367, 2019.

[11] J. Hong, Y. Liu, and J. Yin, "Modulation strategy for optimized transient performance of dual active bridge converter under reverse of power flow direction," in *Proc. IEEE Int. Conf. Ind. Technol.*, 2019, pp. 510–514.

[12] J. Lu and J. Yin, "Unified phase shift control strategy to optimize transient current response in a dual active bridge DC-DC converter during unidirectional and bidirectional power flow changes," in *Proc. IEEE 9th Int. Power Electron. Motion Control Conf.*, 2020, pp. 2599–2604.

[13] B. Zhao, Q. Song, W. Liu, and Y. Zhao, "Transient DC bias and current impact effects of high-frequency-isolated bidirectional DC–DC converter in practice," *IEEE Trans. Power Electron.*, vol. 31, no. 4, pp. 3203–3216, Apr. 2016.

[14] P. Yao, X. Jiang, P. Xue, S. Ji, and F. Wang, "Flux balancing control of ungapped nanocrystalline core-based transformer in dual active bridge converters," *IEEE Trans. Power Electron.*, vol. 35, no. 11, pp. 11463–11474, Nov. 2020.

[15] A. K. Bhattacharjee, S. M. Tayebi, and I. Batarseh, "Fast response dual active bridge converter with elimination of transient DC offset by intermediate asymmetric modulation," in *Proc. IEEE Energy Convers. Congr. Expo.*, 2018, pp. 637–642.

[16] K. Takagi and H. Fujita, "Dynamic control and performance of a dual-active-bridge DC–DC converter," *IEEE Trans. Power Electron.*, vol. 33, no. 9, pp. 7858–7866, Sep. 2018.

[17] K. Li, Y. Wang, J. Xu, J. Wang, R. Li, and C. Lv, "A novel control method for eliminating dc bias in dual-active-bridge DC-DC converters," in *Proc. IEEE Int. Power Electron. Appl. Conf. Expo.*, 2018, pp. 1–6.

[18] M. Wattenberg, U. Schwalbe, and M. Pfost, "Impact of dc-bias on dual active bridge control and how to avoid it," in *Proc. 21st Eur. Conf. Power Electron. Appl.*, 2019, pp. P.1–P.8.

[19] D.-D. Nguyen, K. Yukita, G. Fujita, and M. C. Ta, "A simple dc bias elimination technique for dual-active-bridge dc/dc converters," in *Proc. 10th Int. Conf. Power Electron. ECCE Asia*, 2019, pp. 1–6.

[20] C. Sun and X. Li, "Fast transient modulation for a step load change in a dual-active-bridge converter with extended-phase-shift control," *Energies*, vol. 11, no. 6, 2018, Art. no. 1569.

[21] C. Sun, X. Li, and S.-Z. Zhou, "Transient current control for a step load change in a dual-active-bridge converter," *Electron. Lett.*, vol. 54, no. 22, pp. 1290–1292, 2018.

[22] Q. Bu, H. Wen, J. Wen, Y. Hu, and Y. Du, "Transient DC bias elimination of dual-active-bridge DC–DC converter with improved triple-phase-shift control," *IEEE Trans. Ind. Electron.*, vol. 67, no. 10, pp. 8587–8598, Oct. 2020.

[23] Q. Bu, H. Wen, H. Shi, Y. Hu, and Y. Yang, "Universal transient DC-bias current suppression strategy in dual-active-bridge converters for energy storage systems," *IEEE Trans. Transport. Electrific.*, vol. 7, no. 2, pp. 509–526, Jun. 2021.

[24] J. Hu, S. Cui, D.v. d. Hoff, and R. W. De Doncker, "Generic dynamic phase-shift control for bidirectional dual-active bridge converters," *IEEE Trans. Power Electron.*, vol. 36, no. 6, pp. 6197–6202, Jun. 2021.

[25] F. An, W. Song, K. Yang, N. Hou, and J. Ma, "Improved dynamic performance of dual active bridge DC–DC converters using mpc scheme," *IET Power Electron.*, vol. 11, no. 11, pp. 1756–1765, 2018.

[26] Z. Xiao, W. Lei, G. Gao, Y. Cui, Q. Kang, and M. Wang, "Transient current constraint of dab converter based on model predictive control," in *Proc. IEEE 9th Int. Power Electron. Motion Control Conf.*, 2020, pp. 203–207.

[27] H. Bai, C. Mi, C. Wang, and S. Gargies, "The dynamic model and hybrid phase-shift control of a dual-active-bridge converter," in *Proc. 34th Annu. Conf. IEEE Ind. Electron.*, 2008, pp. 2840–2845.

[28] S. Dutta, S. Hazra, and S. Bhattacharya, "A digital predictive current-mode controller for a single-phase high-frequency transformer-isolated dual-active bridge DC-to-DC converter," *IEEE Trans. Ind. Electron.*, vol. 63, no. 9, pp. 5943–5952, Sep. 2016.

[29] G. G. Oggier, M. Ordonez, J. M. Galvez, and F. Luchino, "Fast transient boundary control and steady-state operation of the dual active bridge converter using the natural switching surface," *IEEE Trans. Power Electron.*, vol. 29, no. 2, pp. 946–957, Feb. 2014.

[30] Z. Shan, J. Jatskevich, H. H. Iu, and T. Fernando, "Simplified load-feedforward control design for dual-active-bridge converters with current-mode modulation," *IEEE Trans. Emerg. Sel. Topics Power Electron.*, vol. 6, no. 4, pp. 2073–2085, Dec. 2018.

[31] Z. Ji, Q. Wang, D. Li, and Y. Sun, "Fast DC-bias current control of dual active bridge converters with feedforward compensation," *IEEE Trans. Circuits Syst. II: Exp. Briefs*, vol. 67, no. 11, pp. 2587–2591, Nov. 2020.

[32] S. Wei, Z. Zhao, K. Li, L. Yuan, and W. Wen, "Deadbeat current controller for bidirectional dual-active-bridge converter using an enhanced SPS modulation method," *IEEE Trans. Power Electron.*, vol. 36, no. 2, pp. 1274–1279, Feb. 2021.

[33] Y. Xiao, Z. Zhang, X. Mao, K. T. Manez, and M. A. E. Andersen, "Power plateau and anti-power phenomenon of dual active bridge converter with phase-shift modulation," in *Proc. IEEE Appl. Power Electron. Conf. Expo.*, 2018, pp. 1871–1875.

[34] K. Takagi and H. Fujita, "Dynamic control and dead-time compensation method of an isolated dual-active-bridge DC-DC converter," in *Proc. 17th Eur. Conf. Power Electron. Appl.*, 2015, pp. 1–10.

[35] S. Buso and P. Mattavelli, *Digital Control in Power Electronics*, 2nd ed. San Rafael, CA, USA: Morgan & Claypool, 2015.

Chuan Sun (Student Member, IEEE) received the B.Eng. degree in electronic and information engineering from the North University of China, Taiyuan, China, in 2015 and the M.Sc. degree in information technology from the Macau University of Science and Technology, Macau, China, in 2017. He is currently working toward the Ph.D. degree in power electronics with The Hong Kong Polytechnic University, Hong Kong, China.

From 2017 to 2018, he was an Electronic Engineer with the Hangzhou Livoltek Power Company, Ltd., Hangzhou, China. His research interests include developing advanced modulation and control strategies for bidirectional resonant and nonresonant dual-active-bridge dc–dc converters.

Xingyue Jiang is currently working toward the Ph.D. degree in electronic and information engineering with The Hong Kong Polytechnic University, Hong Kong, China.

His research interests include peer-to-peer energy trading, energy path planning, and energy Internet.

Junwei Liu (Member, IEEE) received the B.Eng. degree in water conservancy and hydropower engineering from the Huazhong University of Science and Technology, Wuhan, China, in 2012 and the Ph.D. degree from the Department of Electrical Engineering, The Hong Kong Polytechnic University, Hong Kong, in 2018.

He is currently a Research Fellow with the Department of Electronic and Information Engineering, The Hong Kong Polytechnic University. His research interests include wireless power transfer, power factor correction, and ac–dc single-stage topologies.

Lingling Cao (Member, IEEE) received the B.S. and M.S. degrees in electrical engineering from the Nanjing University of Aeronautics and Astronautics, Nanjing, China, in 2008 and 2011, respectively, and the Ph.D. degree from The Hong Kong Polytechnic University, Hong Kong, in 2015.
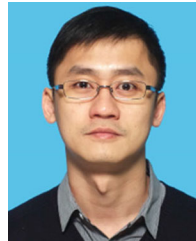
She is currently an Assistant Professor with the Harbin Institute of Technology, Shenzhen, China. Her research interests include power converter topologies and control strategies for renewable energy systems.

Yongheng Yang (Senior Member, IEEE) received the B.Eng. degree in electrical engineering and automation from Northwestern Polytechnical University, Xi'an, China, in 2009 and the Ph.D. degree in energy technology (power electronics and drives) from Aalborg University, Aalborg, Denmark, in 2014.

He was a Postgraduate Student with Southeast University, Nanjing, China, from 2009 to 2011. In 2013, he was a Visiting Scholar with Texas A&M University, College Station, TX, USA. During 2014–2020, he was with the Department of Energy Technology, Aalborg University, where he became a Tenured Associate Professor in 2018. In January 2021, he joined Zhejiang University, Hangzhou, China, as a ZJU100 Professor. His research focuses on the grid-integration of photovoltaic systems and control of power converters, in particular, the grid-forming technologies.

Dr. Yang was the Chair of the IEEE Denmark Section (2019– 2020). He is currently an Associate Editor for several IEEE Transactions. He was the recipient of the 2018 IET Renewable Power Generation Premium Award and was an Outstanding Reviewer for the IEEE TRANSACTIONS ON POWER ELECTRONICS in 2018. He was the recipient of the 2021 Richard M. Bass Outstanding Young Power Electronics Engineer Award from the IEEE Power Electronics Society (PELS) and the 2022 Isao Takahashi Power Electronics Award. In addition, he was also a recipient of two IEEE Best Paper Awards. He has been included on the list of Highly Cited Chinese Researchers by Elsevier in 2022. He is currently the Secretary of the IEEE PELS Technical Committee on Sustainable Energy Systems and a Council Member of the China Power Supply Society.

K. H. Loo (Member, IEEE) received the B.Eng. (Hons.) and Ph.D. degrees in electronic engineering from the University of Sheffield, Sheffield, U.K., in 1999 and 2002, respectively.

From 2002 to 2004, he was with the Japan Society for the Promotion of Science Postdoctoral Fellow with Ehime University, Matsuyama, Japan. Since 2006, he has been with The Hong Kong Polytechnic University, Hong Kong, where he is currently an Associate Professor with the Department of Electronic and Information Engineering. His research interests include power electronics for renewable energy systems.

Dr. Loo has been an Associate Editor for the IEEE TRANSACTIONS ON ENERGY CONVERSION since 2013 and IEEE OPEN JOURNAL OF CIRCUITS AND SYSTEMS since 2019, and a Reviewer for various international journals and conferences. He is currently the Chair of the Power Electronics and Control Subcommittee of the IEEE Technical Committee on Transportation Electrification.